

Resource-efficient equivariant quantum convolutional neural networks

Koki Chinzei,^{*} Quoc Hoan Tran, Yasuhiro Endo, and Hiroataka Oshima

Quantum Laboratory, Fujitsu Research, Fujitsu Limited, 4-1-1 Kawasaki, Kanagawa 211-8588, Japan

(Dated: October 3, 2024)

Equivariant quantum neural networks (QNNs) are promising quantum machine learning models that exploit symmetries to provide potential quantum advantages. Despite theoretical developments in equivariant QNNs, their implementation on near-term quantum devices remains challenging due to limited computational resources. This study proposes a resource-efficient model of equivariant quantum convolutional neural networks (QCNNs) called equivariant split-parallelizing QCNN (sp-QCNN). Using a group-theoretical approach, we encode general symmetries into our model beyond the translational symmetry addressed by previous sp-QCNNs. We achieve this by splitting the circuit at the pooling layer while preserving symmetry. This splitting structure effectively parallelizes QCNNs to improve measurement efficiency in estimating the expectation value of an observable and its gradient by order of the number of qubits. Our model also exhibits high trainability and generalization performance, including the absence of barren plateaus. Numerical experiments demonstrate that the equivariant sp-QCNN can be trained and generalized with fewer measurement resources than a conventional equivariant QCNN in a noisy quantum data classification task. Our results contribute to the advancement of practical quantum machine learning algorithms.

I. INTRODUCTION

Demonstrating practical quantum advantages is a significant challenge in quantum information science. While several quantum algorithms, such as Shor’s factoring [1] and Grover’s search [2], are believed to achieve this goal, they require a large-scale fault-tolerant quantum computer, which will prevent the early realization of quantum advantages [3]. Given this situation, numerous studies have focused on developing quantum algorithms that can be implemented on near-term quantum devices [4]. One promising approach is using variational quantum algorithms (VQAs), where the parameterized quantum circuit (PQC) is optimized to solve a given problem with quantum and classical computers [5]. The VQAs apply to various tasks, such as finding the ground and excited states of Hamiltonian [6], learning an unknown function from data (i.e, quantum machine learning, QML) [7–10], and solving combinatorial optimization problems [11]. However, several obstacles exist that prevent VQAs from achieving quantum advantages. The most critical issue in VQAs is the poor trainability of PQCs. This is often due to barren plateaus where the flat landscape of the cost function causes the optimization process to fail [12–15]. Although many methods have been proposed to avoid barren plateaus [16], completely resolving this issue is still challenging.

Symmetry is crucial for addressing these major issues of VQAs. In particular, geometric quantum machine learning (GQML) is a promising direction that leverages the geometric structure (e.g., symmetry) of data to solve machine learning tasks with high scalability [17–25]. In GQML, the symmetry of a problem is encoded into an equivariant quantum neural network (QNN) as an inductive bias, reducing the parameter space to be searched

and thus leading to high trainability and generalization. For instance, permutation equivariant QNNs were theoretically proven not to show barren plateaus and to improve the generalization performance [26]. The theory of equivariant QNNs has been extended to several circuit models [24], including the quantum convolutional neural network (QCNN) [27, 28]. The QCNN is a representative circuit model due to its high trainability and feasibility [29]. It consists of convolutional (C), pooling (P), and fully connected (FC) layers, as shown in Fig. 1 (a), and its hierarchal structure allows for efficient learning of data features at various length scales [27, 28]. The equivariant QCNN further advances its potential, bringing the realization of practical quantum advantages closer [24].

Despite theoretical developments in equivariant QNNs, the high computational cost of QNNs (i.e., many repetitions of measurements during training QNNs) makes it challenging to implement them on resource-limited near-term quantum devices [30–32]. Solving large-scale problems requires large amounts of training data for high generalization, expressive quantum models for high accuracy, and many measurement shots to accurately estimate expectation values, resulting in substantial computational costs. Recently, an alternative model of equivariant QCNNs, split-parallelizing QCNN (sp-QCNN), has been proposed to reduce the measurement cost in expectation value estimation [33]. The sp-QCNN splits the quantum circuit into multiple branches at the pooling layers instead of discarding the qubits [see Fig. 1 (c)]. This splitting structure maximizes the use of the qubit resource and is thus more efficient than the conventional QCNNs in terms of the number of measurement shots required to achieve a certain accuracy in estimating the expectation value of an observable. Therefore, the sp-QCNN is especially promising for near-term quantum devices with limited computational resources. Nevertheless, the previous study [33] has focused only on situations where the input data is translationally symmetric,

^{*} chinzei.koki@fujitsu.com

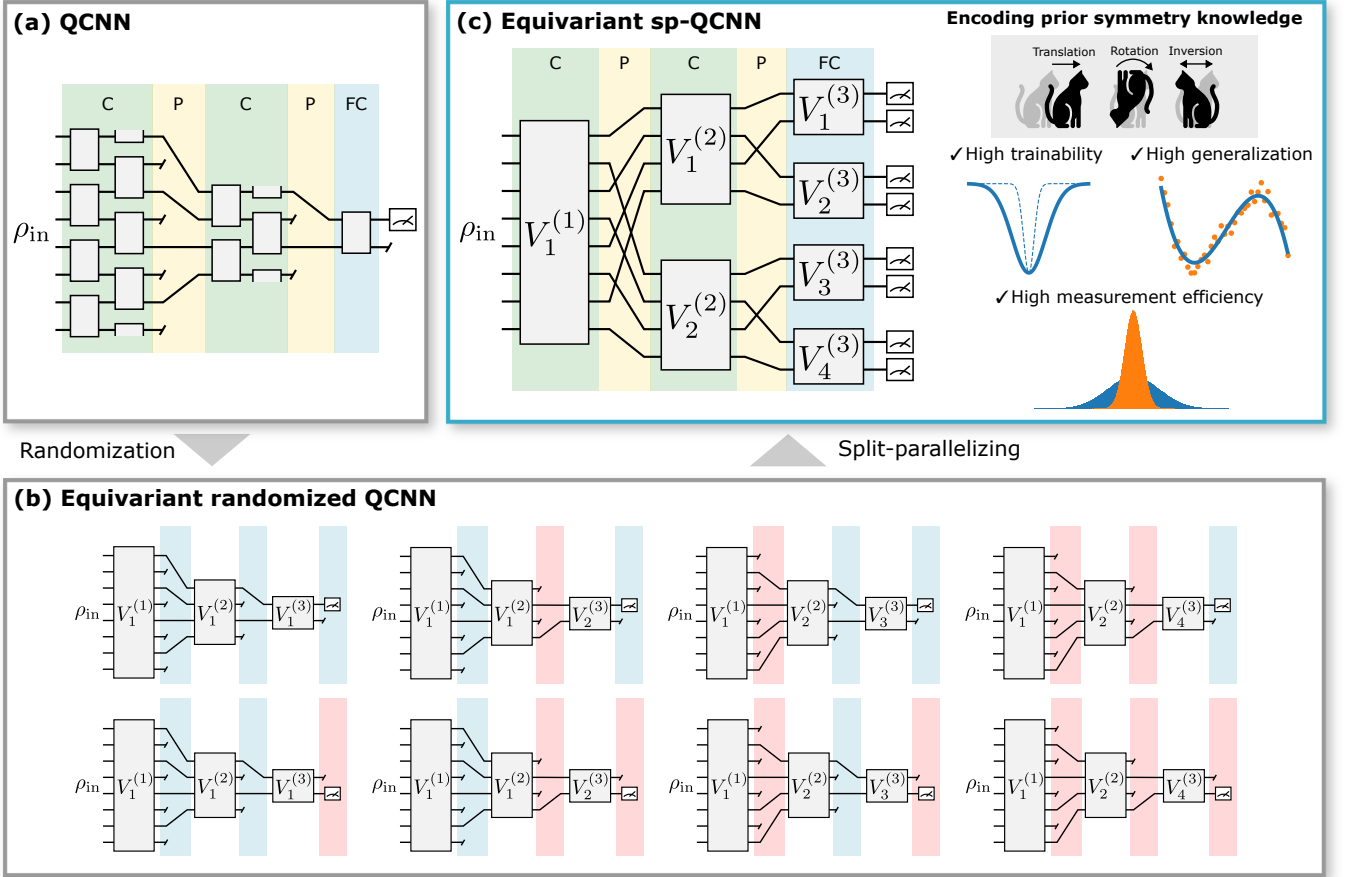


FIG. 1. Basic structures of (a) conventional QCNN [28], (b) equivariant randomized QCNN [24], and (c) equivariant sp-QCNN. (a) In the conventional QCNN, some qubits are discarded at each pooling layer, and the remaining qubits are measured at the end of the circuit. (b) The equivariant randomized QCNN randomly chooses which qubits to discard at each pooling layer to ensure the equivariance. The blue (red) bars indicate the pooling layer that discards even-(odd)-numbered qubits. (c) The equivariant sp-QCNN splits the circuit to impose the equivariance rather than discarding the qubits. This splitting structure with equivariance results in high trainability, generalization, and measurement efficiency.

limiting the range of applications. For example, chemical molecules, a major target in quantum computation, lack translational symmetry (though they possess other symmetries, such as rotations and inversions).

In this work, we propose the framework of equivariant sp-QCNNs for general symmetries beyond translational symmetry and theoretically elucidate their practical advantages. Our model encodes general symmetries into the quantum circuit to ensure equivariance by splitting the circuit based on the symmetry. This equivariance leads to high trainability and generalization as in the conventional equivariant QCNN. Furthermore, the splitting structure effectively parallelizes QCNNs to improve the measurement efficiency by a factor of $\mathcal{O}(n)$ for general symmetries compared to the conventional model, where n is the number of qubits. Our model also inherits the high trainability of QCNNs and does not suffer from barren plateaus. Table I summarizes the performance of three types of QCNNs, displaying that our model can simultaneously achieve high trainability, generalization, and

measurement efficiency by incorporating the equivariance into the splitting structure of the circuit. To leverage these advantages, we present a group-theoretical method for constructing equivariant sp-QCNNs, which provides the theoretical basis for general model design. To demonstrate the high performance of equivariant sp-QCNNs, we apply our model to the classification task of noisy quantum data with square lattice symmetry. The result shows that the high measurement efficiency of the equivariant sp-QCNN suppresses the statistical error in estimating the expectation value, accelerating the training process compared to a conventional equivariant QCNN. Moreover, the equivariant sp-QCNN can achieve high classification accuracy with fewer training data than a non-equivariant model, indicating the high generalization of our model.

The remainder of this paper is organized as follows. First, Sec. II provides a concise overview of QCNNs and equivariant QNNs. Section III formulates the equivariant sp-QCNN and shows its high measurement efficiency in

Model	Trainability	Generalization	Measurement efficiency
QCNN [28]	–	–	–
Equivariant randomized QCNN [24]	High	High	–
Equivariant sp-QCNN (this work)	High	High	High

TABLE I. Trainability, generalization, and measurement efficiency of QCNNs. The hyphen indicates that the performance is comparable to the conventional QCNN.

estimating the expectation value of an observable and its gradient compared to the conventional equivariant QCNN. We also prove that the sp-QCNN does not suffer from barren plateaus under modest assumptions. Section IV introduces a group-theoretical method for constructing the equivariant sp-QCNNs and provides the theoretical basis for general model design. Section V numerically demonstrates the effectiveness of the equivariant sp-QCNN, showing that it outperforms conventional equivariant and non-equivariant QCNNs when the amounts of measurement resources and data are limited. Finally, Sec. VI summarizes our proposal and results and discusses potential future research directions.

II. QUANTUM CONVOLUTIONAL NEURAL NETWORKS AND EQUIVARIANCE

This section concisely reviews QCNNs and equivariant QNNs. In particular, we introduce the randomized model of equivariant QCNN.

A. Quantum convolutional neural network

The QCNN is a promising QNN architecture inspired by the classical convolutional neural network (CNN) [34–36]. This model applies to a variety of machine learning tasks, such as quantum phase recognition [37–39], high energy event classification [40, 41], and quantum error-correcting code optimization [28]. Similar to the CNN, the QCNN has a hierarchical structure consisting of three types of layers: convolutional, pooling, and fully connected layers [27, 28]. The convolutional layers use local unitary gates to extract the local features of the input data, and the pooling layers discard some qubits to coarse-grain the quantum information. After alternately applying the two types of layers, one performs the fully connected transformation and then measures the remaining qubits to obtain an output. In supervised learning, the unitary gates in the convolutional and fully connected layers are optimized to represent the correct input-output relationship.

The high feasibility and trainability of QCNNs show promise for achieving quantum advantages. Since the number of qubits n in the QCNN decreases exponentially with each pooling layer, the circuit depth is $\mathcal{O}(\log n)$. This logarithmic depth leads to easy implementation in near-term quantum devices where the number of possible gate operations is limited. Moreover, it is known that the

QCNN does not suffer from barren plateaus [12–15], the exponentially flat landscape of the cost function, due to the logarithmic circuit depth and the localities of unitary operations and observables [29]. This implies the high scalability of QCNNs.

Despite these promising properties, the high measurement resource requirement for training QCNNs presents practical difficulties. Given that the QCNN has $\mathcal{O}(n) + \mathcal{O}(n/2) + \mathcal{O}(n/4) + \dots = \mathcal{O}(n)$ parameters, it generally requires $\mathcal{O}(nN_{\text{train}}N_{\text{epoch}}N_{\text{shot}})$ measurement shots for training in total, where N_{train} is the number of training data, N_{epoch} is the maximum epoch of training, and N_{shot} is the number of measurement shots used per circuit. Therefore, addressing large-scale problems that involve many qubits and a substantial amount of data is difficult in practice. In this work, we demonstrate that the equivariant sp-QCNN can ideally reduce N_{shot} by a factor of $\mathcal{O}(1/n)$ for general symmetries, thus alleviating the measurement resource requirement.

B. Equivariant QNN

The GQML based on equivariant QNNs has recently emerged as a potential solution to some critical QML problems related to trainability and generalization [17–25]. It exploits the symmetry of a problem as an inductive bias and provides a problem-tailored circuit model, typically an equivariant QNN. For example, in supervised learning, the GQML assumes the label symmetry of the learning problem. The label symmetry arises in various problems, such as image recognition, graph classification, and quantum physics. To define the label symmetry, let ρ be an input density matrix and $f(\rho)$ be a target function to be learned. Then, the label symmetry G is defined as

$$f(\rho) = f(U_g \rho U_g^\dagger) \quad \forall g \in G, \forall \rho, \quad (1)$$

where U_g is a unitary representation of the group G .

The GQML encodes this label symmetry into a quantum circuit as an equivariant QNN to improve trainability and generalization. The equivariant QNN is a parametrized quantum circuit $U(\boldsymbol{\theta})$ that is invariant under the action of G :

$$[U(\boldsymbol{\theta}), U_g] = 0 \quad \forall g \in G. \quad (2)$$

This symmetry leads to the equivariance between input and output quantum states, $U(\boldsymbol{\theta})[U_g \rho U_g^\dagger]U^\dagger(\boldsymbol{\theta}) = U_g[U(\boldsymbol{\theta})\rho U^\dagger(\boldsymbol{\theta})]U_g^\dagger$. That is, applying the symmetry

operation U_g to the input state ρ is identical to applying it to the output state $U(\boldsymbol{\theta})\rho U^\dagger(\boldsymbol{\theta})$. Given this equivariant QNN and a G -symmetric observable O (i.e., $[O, U_g] = 0$), the label symmetry of Eq. (1) always holds with $f(\rho) = \text{tr}[U(\boldsymbol{\theta})\rho U^\dagger(\boldsymbol{\theta})O]$.

The equivariant QNN can be designed in several ways [21, 24], such as the twirling, nullspace, and Choi operator methods, which have been applied to various QNN models. In QCNNs, however, the pooling layers generally break spatial symmetries (e.g., translation, rotation, and inversion of qubit positions) by discarding some qubits in the middle of the circuit, which prevents the straightforward implementation of spatially equivariant QCNNs. To circumvent such difficulties, a randomized technique was introduced to impose the spatial equivariance of the pooling layer [24]. This technique randomly chooses which qubits to discard in each pooling layer for each measurement shot based on a given symmetry. For example, for translational symmetry T (e.g., $T|10\dots 0\rangle = |010\dots 0\rangle$), the equivariance is achieved by randomly choosing which to discard even- or odd-numbered qubits every measurement shot. Then, the quantum operation for an input ρ is given by $\rho \rightarrow (U_e \rho U_e^\dagger + U_o \rho U_o^\dagger)/2$, where $U_{e(o)}$ is the unitary operation acting on the even-(odd-)numbered qubits after the pooling layer with $TU_e T^\dagger = U_o$ [see Fig. 1 (b)]. In other words, the randomized technique classically mixes the multiple QCNNs to ensure the equivariance.

The sp-QCNN is an alternative approach that coherently executes the multiple QCNNs to achieve the equivariance [33]. As shown in Fig. 1 (c), the sp-QCNN splits the circuit in the pooling layers instead of randomly selecting which qubits to discard. This splitting structure maximally makes use of the qubit resource, improving the measurement efficiency in estimating the expectation value of an observable compared to the randomized method. In Ref. [33], the high measurement efficiency of sp-QCNN for translationally symmetric data was demonstrated based on the effective parallelization of conventional QCNN. However, the previous work focused only on the translationally symmetric data, limiting the applicability of sp-QCNNs. This work extends the concept of sp-QCNNs to equivariant sp-QCNNs and develops their theoretical framework for general symmetries.

III. EQUIVARIANT SP-QCNN

This section formulates the equivariant sp-QCNN and shows that it improves the measurement efficiency by a factor of $\mathcal{O}(n)$ compared to the conventional randomized QCNN. We also prove that the sp-QCNN does not suffer from barren plateaus under modest assumptions, as do conventional QCNNs.

A. Model

The equivariant sp-QCNN is a resource-efficient model of equivariant QCNNs, consisting of circuit splitting and unitary operations [see Fig. 1 (c)]. Here, let $Q_{\text{bit}} = [n]$ be the set of qubits whose element corresponds to each qubit (throughout this paper, we denote $[a] = \{1, 2, \dots, a\}$ with an integer a). We write the circuit splitting in the ℓ th layer as a partition of Q_{bit} :

$$Q_{\text{bit}} = \bigsqcup_{i=1}^{s_\ell} Q_i^{(\ell)}, \quad (3)$$

where $Q_i^{(\ell)}$ is a subset of the qubits representing the i th branch of the ℓ th layer, s_ℓ is the number of branches in the ℓ th layer, and \bigsqcup denotes the disjoint union. Note that the branches are not overlapped [i.e., $Q_i^{(\ell)} \cap Q_j^{(\ell)} = \emptyset$ for $i \neq j$] and that they cover all qubits [i.e., $\bigsqcup_i Q_i^{(\ell)} = Q_{\text{bit}}$]. We assume that each branch in the $(\ell + 1)$ th layer is connected to a corresponding single branch in the ℓ th layer:

$$\forall i, \exists j \text{ s.t. } Q_i^{(\ell+1)} \subseteq Q_j^{(\ell)}. \quad (4)$$

To clarify, each branch can be split but cannot be merged to another branch. As discussed later, this splitting structure contributes to the effective parallelization of QCNNs.

The unitary of the entire circuit is given by

$$U = \prod_{\ell=1}^L V^{(\ell)}, \quad (5)$$

where $V^{(\ell)}$ is the unitary of the ℓ th convolutional layer. The convolutional layer $V^{(\ell)}$ is decomposed into s_ℓ unitaries $V_i^{(\ell)}$, each of which acts on $Q_i^{(\ell)}$ as

$$V^{(\ell)} = \prod_{i=1}^{s_\ell} V_i^{(\ell)}. \quad (6)$$

Since each $V_i^{(\ell)}$ acts on different qubits, they are mutually commutative: $[V_i^{(\ell)}, V_j^{(\ell)}] = 0$.

When the label symmetry G of a problem is known in advance, the equivariance for the symmetry can help improve the trainability and generalization of the quantum model. Here, the G -equivariance of sp-QCNN at each layer is defined as

$$[V^{(\ell)}, U_g] = 0 \quad \forall g \in G. \quad (7)$$

Along with a G -symmetric observable O (i.e., $[U_g, O] = 0 \quad \forall g \in G$), this equivariance leads to the label symmetry of $f(\rho) = \text{Tr}[U\rho U^\dagger O]$ as $f(U_g \rho U_g^\dagger) = f(\rho)$ for $\forall \rho$ and $\forall g \in G$. This equivariance effectively reduces the circuit expressivity without sacrificing accuracy, thus improving trainability and generalization.

B. Measurement efficiency

In addition to improving trainability and generalization, our model exhibits higher measurement efficiency than the conventional randomized QCNN. This high measurement efficiency comes from the effective parallelization of QCNNs. To show this, let us examine the randomized model that corresponds directly to the equivariant sp-QCNN characterized by $Q_i^{(\ell)}$ and $V_i^{(\ell)}$. The randomized QCNN randomly selects which branch to remain in each pooling layer for every measurement shot [Fig. 1 (b)]. Therefore, the ℓ th convolutional layer classically mixes the input ρ as $\rho \rightarrow \sum_{i=1}^{s_\ell} V_i^{(\ell)} \rho V_i^{(\ell)\dagger} / s_\ell$. The expectation value of a local observable $O = \sum_{i=1}^n O_i / n$ (O_i an observable acting only on the i th qubit) in the randomized QCNN is defined as the classical summation of the expectation values for several circuits:

$$\langle O \rangle_{\text{RD}} = \frac{1}{n} \sum_{i=1}^n \text{tr} \left[B_i \rho B_i^\dagger O_i \right], \quad (8)$$

where $\langle \cdot \rangle_{\text{RD}}$ is the expectation value in the randomized QCNN, and $B_i = V_{i_L}^{(L)} \cdots V_{i_1}^{(1)}$ denotes the executed circuit of the randomized QCNN involving the i th qubit. Here, B_i can also be viewed as the subcircuit (or backward lightcone) of sp-QCNN associated with the i th qubit. In other words, the randomized QCNN chooses one of the subcircuits B_i randomly for every measurement shot, taking an average over the outputs of all the subcircuits.

In the absence of statistical errors in measurements, the sp-QCNN produces the same result as the randomized model. One can show this by

$$\begin{aligned} \langle O \rangle_{\text{sp}} &= \text{tr}(U \rho U^\dagger O) \\ &= \frac{1}{n} \sum_{i=1}^n \text{tr}(U \rho U^\dagger O_i) \\ &= \frac{1}{n} \sum_{i=1}^n \text{tr}(B_i \rho B_i^\dagger O_i) \\ &= \langle O \rangle_{\text{RD}}, \end{aligned} \quad (9)$$

where $\langle \cdot \rangle_{\text{sp}}$ is the expectation value in the sp-QCNN. In the third line, we have used $U^\dagger O_i U = B_i^\dagger O_i B_i$, which is derived from the hierarchical circuit structure and the locality of O_i . This result suggests that the sp-QCNN can coherently execute all the subcircuits in parallel, leading to higher measurement efficiency than the randomized model. Note that all randomized models do not have corresponding sp-QCNNs because the branches are prohibited from overlapping in sp-QCNNs [i.e., $Q_i^{(\ell)} \cap Q_j^{(\ell)} = \emptyset$ for $i \neq j$].

The coherent parallelization of sp-QCNN enables us to obtain n times more measurement outcomes per circuit execution than the randomized model, potentially leading to the $\mathcal{O}(n)$ times improvement of measurement

efficiency. This high measurement efficiency reduces the number of measurement shots required to achieve a certain accuracy in estimating the expectation value of an observable. Note that our model does not exactly improve the measurement efficiency by a factor of n in general because the n measurement outcomes are correlated to each other due to the quantum entanglement of the output state. For example, when the output state is the GHZ state $|\psi\rangle = (|00\dots\rangle + |11\dots\rangle) / \sqrt{2}$, the sp-QCNN cannot improve the measurement efficiency because the n measurement outcomes are completely correlated and only one-bit information is available every measurement shot. In contrast, when the output state is random, the sp-QCNN can improve the measurement efficiency by a factor of $\mathcal{O}(n)$ because the n measurement outcomes are not correlated effectively [33]. Given that the learning process in actual QML problems is generally complicated and can be considered approximately random (at least at the beginning of learning when the parameters are randomly initialized), we expect the sp-QCNN to be resource-efficient. In Sec. V, we will verify that the sp-QCNN can considerably improve the measurement efficiency in a specific classification task.

C. Gradient measurement efficiency

The equivariant sp-QCNN also improves the measurement efficiency in the gradient estimation. In VQAs, solving large-scale problems requires an efficient training algorithm. Among various training algorithms, the gradient-based optimization method is promising, where the parameters are updated based on the gradient of the loss function L as $\theta \rightarrow \theta - \eta \nabla L$ (η is the learning rate). However, the gradient estimation needs a high computational cost in quantum computing [32]. Therefore, improving the gradient measurement efficiency is crucial for the implementation of large-scale models.

The equivariant sp-QCNN allows us to execute the randomized QCNN in parallel even in the gradient measurement. To show this, we consider the derivative of the expectation value of a local observable $O = \sum_{i=1}^n O_i / n$ in the sp-QCNN [see Eq. (9)]:

$$\partial_\mu \langle O \rangle_{\text{sp}} = \frac{1}{n} \sum_{i=1}^n \partial_\mu \text{tr}(B_i \rho B_i^\dagger O_i), \quad (10)$$

where ∂_μ denotes $\partial / \partial \theta_\mu$. Suppose that θ_μ is a parameter in a branch $Q_\mu \subseteq Q_{\text{bit}}$ [e.g., if θ_μ is the parameter of $V_i^{(\ell)}$, $Q_\mu = Q_i^{(\ell)}$]. Then, we have $\partial_\mu \text{tr}(B_i \rho B_i^\dagger O_i) = 0$ for $i \notin Q_\mu$ in Eq. (10) because B_i does not depend on θ_μ due to the hierarchical structure. Hence, the derivative is written as

$$\partial_\mu \langle O \rangle_{\text{sp}} = \frac{1}{n} \sum_{i \in Q_\mu} \partial_\mu \text{tr}(B_i \rho B_i^\dagger O_i), \quad (11)$$

Using the parameter-shift rule [8, 42], we can measure

the derivative as

$$\partial_\mu \langle O \rangle_{\text{sp}} = \frac{1}{n} \sum_{i \in Q_\mu} \left[\text{tr}(B_{i\mu+\rho} B_{i\mu+}^\dagger O_i) - \text{tr}(B_{i\mu-\rho} B_{i\mu-}^\dagger O_i) \right], \quad (12)$$

where $B_{i\mu\pm}$ is the subcircuit of sp-QCNN in which θ_μ is replaced with $\theta_\mu \pm \pi/4$. The randomized model chooses one of the subcircuits B_i ($i \in Q_\mu$) every circuit execution and measures O_i in the parameter-shifted circuit, thus requiring $2|Q_\mu|$ types of quantum circuits for obtaining the derivative $\partial_\mu \langle O \rangle_{\text{RD}} = \partial_\mu \langle O \rangle_{\text{sp}}$.

The splitting structure of the sp-QCNN enables us to measure the gradient more efficiently. This high efficiency stems from two factors. First, the sp-QCNN can measure all the terms in Eq. (12) with only two types of quantum circuits (i.e., the $\pm\pi/4$ parameter-shifted circuits) by coherently executing B_i ($i \in Q_\mu$) in parallel, which improves the measurement efficiency by a factor of $\mathcal{O}(|Q_\mu|)$. Second, the sp-QCNN can measure different derivatives $\partial_\mu \langle O \rangle$ and $\partial_\nu \langle O \rangle$ simultaneously if θ_μ and θ_ν belong to different branches (i.e., $Q_\mu \cap Q_\nu = \emptyset$). This is due to the fact that, in the Heisenberg picture, the two observables $B_{i\mu\pm}^\dagger O_i B_{i\mu\pm}$ and $B_{j\nu\pm}^\dagger O_j B_{j\nu\pm}$ in Eq. (12) are not overlapped and commute with each other. Therefore, $B_{i\mu\pm}^\dagger O_i B_{i\mu\pm}$ and $B_{j\nu\pm}^\dagger O_j B_{j\nu\pm}$ are simultaneously measurable. This technique allows us to simultaneously measure s_ℓ derivatives for s_ℓ branches in the ℓ th convolutional layer, improving the gradient measurement efficiency by a factor of $\mathcal{O}(s_\ell)$. Combining these two factors, the sp-QCNN achieves the $\mathcal{O}(|Q_\mu|) \times \mathcal{O}(s_\ell) \sim \mathcal{O}(n)$ times improvement of the gradient measurement efficiency (we have used $|Q_\mu| \sim n/s_\ell$ in the ℓ th layer).

We note that the discussions in Secs. III B and III C do not rely on the equivariance of sp-QCNNs. This implies that the high measurement efficiency of sp-QCNNs stems from the splitting structure rather than the equivariance. The equivariant sp-QCNN integrates the splitting structure with the equivariance to simultaneously achieve high trainability, generalization, and measurement efficiency.

D. Absence of barren plateaus

A natural question arises regarding the potential impact of the splitting structure of sp-QCNNs on the high trainability of QCNNs. Specifically, one might wonder if the circuit splitting leads to barren plateaus. We demonstrate this is not the case: the sp-QCNNs do not suffer from barren plateaus as well as conventional QCNNs. For simplicity, we consider a non-equivariant sp-QCNN, denoted by $U(\boldsymbol{\theta})$, and add single qubit rotations $R(\boldsymbol{\alpha}, \boldsymbol{\beta}) = \prod_{j=1}^n R_j(\alpha_j, \beta_j)$ to the end of the circuit, where $R_j(\alpha_j, \beta_j) = e^{-i\alpha_j X_j} e^{-i\beta_j Z_j}$ is a single qubit rotation gate. Therefore, the total unitary of these circuits is given by $U_{\text{tot}}(\boldsymbol{\theta}, \boldsymbol{\alpha}, \boldsymbol{\beta}) = R(\boldsymbol{\alpha}, \boldsymbol{\beta})U(\boldsymbol{\theta})$. Here, we show that $U_{\text{tot}}(\boldsymbol{\theta}, \boldsymbol{\alpha}, \boldsymbol{\beta})$ does not exhibit barren plateaus under an assumption.

We consider a cost function $C(\rho) = \text{Tr}[U_{\text{tot}}\rho U_{\text{tot}}^\dagger O]$ with $O = \sum_j O_j$, where O_j is a local observable acting only on the j th qubit. The cost function is written as the summation of local cost functions $C(\rho) = \sum_j C_j(\rho)$ using $C_j(\rho) = \text{Tr}[U_{\text{tot}}\rho U_{\text{tot}}^\dagger O_j] = \text{Tr}[B_j \rho B_j^\dagger O_j]$, where B_j is the subcircuit of U_{tot} associated with the j th qubit. Here, we assume that $C_j(\rho)$ does not exhibit barren plateaus:

$$\text{Var}[C_j(\rho)] \in \Omega\left(\frac{1}{\text{poly}(n)}\right), \quad (13)$$

where $\text{Var}[A]$ denotes a variance of A in the parameter space. This assumption is reasonable because the subcircuit B_j has the same structure as a conventional QCNN, in which the absence of barren plateaus is proved [29].

By using $\text{Var}[A+B] = \text{Var}[A] + \text{Var}[B] + 2\text{Cov}[A, B]$ and $\text{Cov}[A, B] = E[AB] - E[A]E[B]$, the variance of the total cost function is

$$\begin{aligned} \text{Var}[C(\rho)] &= \sum_j \text{Var}[C_j(\rho)] \\ &+ 2 \sum_{j < k} E[C_j(\rho)C_k(\rho)] \\ &- 2 \sum_{j < k} E[C_j(\rho)]E[C_k(\rho)], \end{aligned} \quad (14)$$

where $\text{Cov}[A, B]$ is the covariance of A and B , and $E[A]$ is the expectation value of A in the parameter space. The first term on the right-hand side is $\Omega(1/\text{poly}(n))$ due to the assumption (13), but the negative correlation of C_j and C_k in the second and third terms may lead to the exponentially small variance of C in general. Below, we show that the second and third terms vanish in our ansatz U_{tot} , proving the absence of barren plateaus.

We first show that the third term on the right-hand side of Eq. (14) vanishes for $U_{\text{tot}}(\boldsymbol{\theta}, \boldsymbol{\alpha}, \boldsymbol{\beta}) = R(\boldsymbol{\alpha}, \boldsymbol{\beta})U(\boldsymbol{\theta})$. The expectation value of C_j is written as

$$E[C_j(\rho)] = \frac{1}{\mathcal{N}} \int d\boldsymbol{\theta} d\boldsymbol{\alpha} d\boldsymbol{\beta} \text{Tr} \left[\rho U_{\text{tot}}^\dagger O_j U_{\text{tot}} \right], \quad (15)$$

where \mathcal{N} is the normalization factor, and the integrals of $\boldsymbol{\alpha}$ and $\boldsymbol{\beta}$ run from 0 to π . We notice that

$$\int_0^\pi d\alpha_j \int_0^\pi d\beta_j R_j^\dagger(\alpha_j, \beta_j) O_j R_j(\alpha_j, \beta_j) = 0 \quad (16)$$

for any O_j expressed as a linear combination of X_j, Y_j and Z_j . Thereby, one can easily show that the integration in Eq. (15) is zero:

$$E[C_j(\rho)] = 0. \quad (17)$$

Thus, the third term in Eq. (14) vanishes. Similarly, the second term in Eq. (14) is written as

$$\begin{aligned} &E[C_j(\rho)C_k(\rho)] \\ &= \frac{1}{\mathcal{N}^2} \int d\boldsymbol{\theta} d\boldsymbol{\alpha} d\boldsymbol{\beta} \text{Tr} \left[\rho U_{\text{tot}}^\dagger O_j U_{\text{tot}} \right] \text{Tr} \left[\rho U_{\text{tot}}^\dagger O_k U_{\text{tot}} \right]. \end{aligned} \quad (18)$$

In this integral, $U_{\text{tot}}^\dagger O_k U_{\text{tot}} = \cdots R_j^\dagger O_k R_j \cdots$ does not depend on α_j and β_j because $R_j(\alpha_j, \beta_j)$ commutes with O_k for $j \neq k$. Therefore, the integration by α_j and β_j acts only on $U_{\text{tot}}^\dagger O_j U_{\text{tot}}$ in Eq. (18). Therefore, given Eq. (16), the second term in Eq. (14) vanishes:

$$E[C_j(\rho)C_k(\rho)] = 0. \quad (19)$$

Combining Eqs. (13), (14), (17), and (19), we obtain

$$\text{Var}[C(\rho)] \in \Omega\left(\frac{1}{\text{poly}(n)}\right), \quad (20)$$

implying that there are no barren plateaus in sp-QCNNs.

While we only focus on the non-equivariant case, we expect that equivariant sp-QCNNs do not suffer from barren plateaus as well. This is due to the fact that the symmetry constraint reduces the circuit expressivity, increasing the variance of the cost function in general [43–45]. We also remark on the necessity of $R(\alpha, \beta)$. Although we have assumed $R(\alpha, \beta)$ for the proof, it will not be necessary for the absence of barren plateaus in most cases because the situation where the final single qubit rotations determine the existence of barren plateaus is rather peculiar. Even if barren plateaus depend on the final single qubit rotations, this does not matter in practice because we can easily avoid barren plateaus only by adding single qubit rotations at the end of the circuit.

IV. SYSTEMATIC CONSTRUCTION OF EQUIVARIANT SP-QCNN

This section introduces a systematic method of constructing equivariant sp-QCNNs. Previous studies have proposed several techniques for designing equivariant QNNs, such as the twirling, the nullspace, and the Choi operator methods [21, 24]. However, as these methods do not assume the constraint of qubit splitting, they are not straightforwardly applicable to spatially equivariant sp-QCNNs that are invariant under spatial operations permuting the qubit positions. Thus, this work provides an alternative method of constructing equivariant sp-QCNNs, called the subgroup method, especially for spatial symmetries.

This section mainly focuses on spatial symmetry G , which is a subgroup of the symmetric group S_n . The symmetric group S_n is defined as the set of all bijective functions from Q_{bit} to Q_{bit} , namely all permutations of qubits. Since G is a subgroup of S_n , G also represents the permutations of qubits, such as rotation, inversion, and translation of the lattice on which the qubits are defined. Based on S_n , the action of $g \in G$ on Q_{bit} is defined as $g(q_i) = q_j$ ($q_i, q_j \in Q_{\text{bit}}$), and the action on a subset $Q_1 \subseteq Q_{\text{bit}}$ is also defined as $g(Q_1) = \{g(q)|q \in Q_1\}$. In addition, the action of G on Q_{bit} naturally leads to a unitary representation U_g on the n -qubits quantum system as $U_g|\sigma_1 \cdots \sigma_n\rangle = |\sigma_{g(1)} \cdots \sigma_{g(n)}\rangle$, where $|\sigma_1 \cdots \sigma_n\rangle$ is a computational basis with $\sigma_j = 0, 1$. We note that

while this section only focuses on spatial symmetries, other types of symmetries (e.g., internal symmetries that do not permute the qubit positions) can be incorporated into our sp-QCNN by appropriately designing the unitary operators on each branch $V_i^{(\ell)}$ with the conventional approaches of equivariant QNNs.

For convenience, we define the following terms:

Definition 1 (G -equivalence of qubits). We say that qubits $q_1, q_2 \in Q_{\text{bit}}$ are G -equivalent and denote $q_1 \sim q_2$ if and only if there exists $g \in G$ such that $g(q_1) = q_2$.

Definition 2 (G -independence of qubits). We say that a subset of qubits $Q_1 \subseteq Q_{\text{bit}}$ is G -independent if and only if $\forall q_1, q_2 \in Q_1$ ($q_1 \neq q_2$) are not G -equivalent.

Definition 3 (G -completeness of qubits). We say that a subset of qubits $Q_1 \subseteq Q_{\text{bit}}$ is G -complete if and only if, for any $q \in Q_{\text{bit}}$, there exists $q_1 \in Q_1$ that is G -equivalent to q .

A. Subgroup and coset

For preliminaries, we briefly review some notions of the group theory used in the subgroup method [46]. Consider a finite group G , where a binary operation $G \times G \rightarrow G$ is defined with associativity, an identity element, and inverse elements. A subset $H \subseteq G$ is called a subgroup of G if H is also a group under the same binary operation as G . In this work, we denote $H \leq G$ if H is a subgroup of G .

Given a subgroup H and an element $g \in G$, the left coset C_g^H is defined as follows:

$$C_g^H = gH = \{gh | h \in H\}. \quad (21)$$

Here, $|C_g^H| = |H|$ holds for all $g \in G$. In what follows, we will refer to left cosets as cosets for simplicity. The definition of cosets readily leads to the fact that a symmetry operation $g \in G$ maps a coset to another one:

$$g(C_{g_1}^H) = gg_1H = g_2H = C_{g_2}^H \quad (22)$$

with $gg_1 = g_2$. An important property of cosets is that different cosets for H either are identical or have no intersection:

$$C_{g_1}^H = C_{g_2}^H \text{ or } C_{g_1}^H \cap C_{g_2}^H = \emptyset \quad (23)$$

with $\forall g_1, g_2 \in G$. Therefore, G is decomposed into $s = |G|/|H|$ cosets as

$$G = \bigsqcup_{i=1}^s C_i^H, \quad (24)$$

where C_i^H denotes the i th coset of H in G . We will use the coset decomposition for systematically constructing equivariant sp-QCNNs.

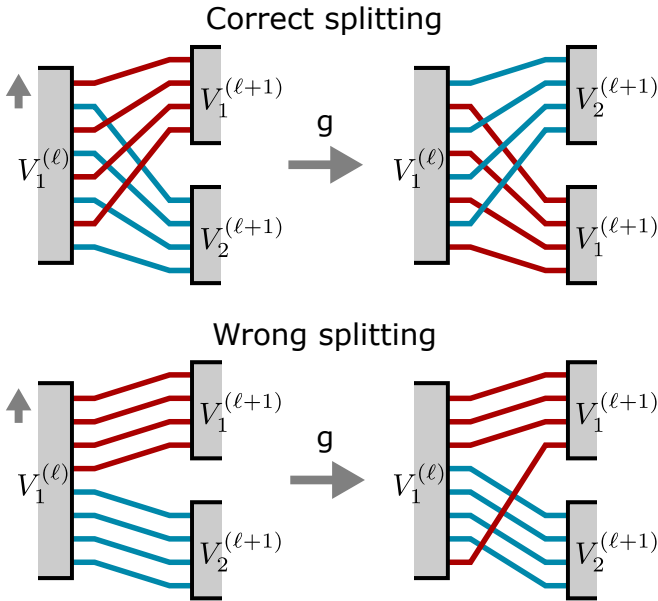


FIG. 2. Correct and wrong examples of circuit splitting for translational symmetry $G = \{T^0, T^1, \dots, T^{n-1}\}$, where T is the translational operation acting as $T(q_i) = q_{i-1}$ (q_i is the i th qubit). In the correct example, the G -invariance holds: $T(Q_1) = Q_2$ with $Q_1 = \{q_1, q_3, q_5, q_7\}$ and $Q_2 = \{q_2, q_4, q_6, q_8\}$. In contrast, the G -invariance does not hold in the wrong example: $T(Q_1) \neq Q_2$ with $Q_1 = \{q_1, q_2, q_3, q_4\}$ and $Q_2 = \{q_5, q_6, q_7, q_8\}$.

B. Subgroup method

Here, we present the subgroup method to systematically construct equivariant sp-QCNNs. This method involves two steps. The first step determines the circuit splitting so that it does not break a given symmetry. Then, as the second step, we design a symmetric unitary operator acting on each branch determined in the first step. Below, we will describe the outline of the subgroup method. The details are provided in Appendix A.

1. Circuit splitting

The first step is appropriately splitting the circuit such that $\forall g \in G$ does not change the splitting structure, i.e. the branches $\mathcal{Q}^{(\ell)} = \{Q_i^{(\ell)}\}_{i=1}^{s_\ell}$. With the aforementioned Eqs. (3) and (4), there are three requirements for the G -equivariant circuit splitting as follows:

1. G -invariance of circuit splitting:

$$g(\mathcal{Q}^{(\ell)}) = \mathcal{Q}^{(\ell)} \text{ for } \forall g \in G. \quad (25)$$

2. Branches do not merge:

$$\forall i, \exists j \text{ s.t. } Q_i^{(\ell+1)} \subseteq Q_j^{(\ell)}. \quad (26)$$

3. Branches are a partition of qubits:

$$Q_i^{(\ell)} \cap Q_j^{(\ell)} = \emptyset \text{ for } i \neq j, \quad (27)$$

$$\bigcup_i Q_i^{(\ell)} = Q_{\text{bit}}. \quad (28)$$

In particular, Eq. (25) means that any symmetry operation can permute the branches but never modify the entire splitting structure, as illustrated in Fig. 2, which is essential for the equivariance.

The subgroup method gives a systematic way of circuit splitting to satisfy Eqs. (25)–(28). The key idea is as follows. We consider a set of subgroups

$$\mathcal{H}^{(\ell)} = \{H_\lambda^{(\ell)}\}_{\lambda=1}^{\Lambda_\ell} \quad (29)$$

and a set of qubit subsets

$$\mathcal{P}^{(\ell)} = \{P_\lambda^{(\ell)}\}_{\lambda=1}^{\Lambda_\ell}, \quad (30)$$

where $H_\lambda^{(\ell)}$ and $P_\lambda^{(\ell)}$ are a subgroup of G and a subset of Q_{bit} , respectively. An integer Λ_ℓ denotes the number of subgroups and subsets for the ℓ th layer. From these $\mathcal{H}^{(\ell)}$ and $\mathcal{P}^{(\ell)}$, we define the following branch:

$$\begin{aligned} Q_{\lambda,i}^{(\ell)} &= C_i^{H_\lambda^{(\ell)}}(P_\lambda^{(\ell)}) \\ &= \left\{ g(q) \mid g \in C_i^{H_\lambda^{(\ell)}}, q \in P_\lambda^{(\ell)} \right\}, \end{aligned} \quad (31)$$

where $C_i^{H_\lambda^{(\ell)}}$ is the i th coset of $H_\lambda^{(\ell)}$ in G . Remarkably, $\mathcal{Q}^{(\ell)} = \{Q_{\lambda,i}^{(\ell)}\}_{\lambda,i}$ constructed in this way is G -invariant, i.e., it satisfies Eq. (25). In fact, one can verify that

$$g(Q_{\lambda,i}^{(\ell)}) = gC_i^{H_\lambda^{(\ell)}}(P_\lambda^{(\ell)}) = C_j^{H_\lambda^{(\ell)}}(P_\lambda^{(\ell)}) = Q_{\lambda,j}^{(\ell)}, \quad (32)$$

where we have used Eq. (22) that the symmetry operation $g \in G$ maps a coset to another one.

Based on this idea, we can find $\mathcal{H}^{(\ell)}$ and $\mathcal{P}^{(\ell)}$ to satisfy the requirements of Eqs. (26)–(28) by choosing them layer by layer. To meet Eq. (26), we determine $\mathcal{H}^{(\ell)}$ and $\mathcal{P}^{(\ell)}$ as follows: for $\forall \lambda \in [\Lambda_{\ell+1}]$, there exists $\lambda' \in [\Lambda_\ell]$ such that

$$H_\lambda^{(\ell+1)} \leq H_{\lambda'}^{(\ell)} \text{ and } P_\lambda^{(\ell+1)} \subseteq P_{\lambda'}^{(\ell)}. \quad (33)$$

As proven in Appendix A 1 b, this condition ensures the requirement of Eq. (26). Moreover, the following conditions are sufficient for the requirements of Eqs. (27) and (28):

$$1. |G(q)|/|H_\lambda^{(\ell)}(q)| = |G|/|H_\lambda^{(\ell)}| \text{ for } \forall q \in P_\lambda^{(\ell)}, \quad (34)$$

$$2. P^{(\ell)} \text{ is } G\text{-independent}, \quad (35)$$

$$3. P^{(\ell)} \text{ is } G\text{-complete}, \quad (36)$$

where we have defined $P^{(\ell)} = \bigsqcup_\lambda P_\lambda^{(\ell)}$. The details are provided in Appendix A 1 c. To summarize, satisfying all requirements of Eqs. (25)–(28) necessitates careful selection of $\mathcal{H}^{(\ell)}$ and $\mathcal{P}^{(\ell)}$ to fulfill the conditions of

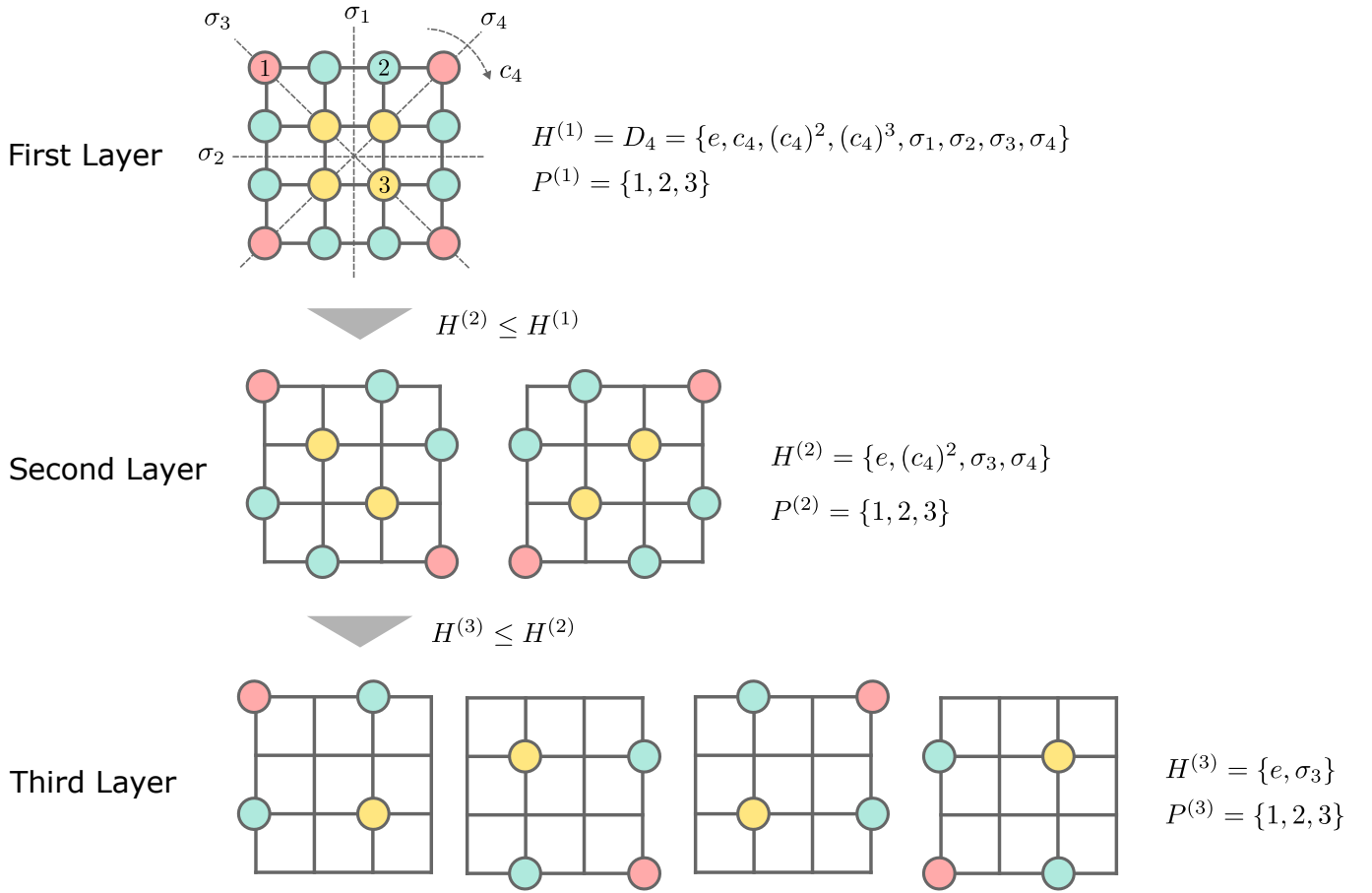


FIG. 3. An example of circuit splitting for $D_4 = \{e, c_4, (c_4)^2, (c_4)^3, \sigma_1, \sigma_2, \sigma_3, \sigma_4\}$ symmetry (e is an identity operator, c_4 is a rotation by $\pi/2$, and σ_i 's are inversion operations around each axis). Each circle represents a qubit, and qubits with the same color are G -equivalent (see Definition 1). We can construct the circuit splitting from a subgroup $H^{(\ell)}$ and a qubit subset $P^{(\ell)}$.

Eqs. (33)–(36). In Appendix A 2, we present a systematic method with proof to determine $\mathcal{H}^{(\ell)}$ and $\mathcal{P}^{(\ell)}$ that satisfy these conditions. This method proceeds layer by layer from $\ell = L$ to $\ell = 1$, ensuring Eqs. (33)–(36) and thus Eqs. (25)–(28) by enumerating all subgroups of G . The computational cost of this method is polynomial in the number of qubits n and, therefore, feasible unless G is not too large to be tractable.

As an example of circuit splitting, let us consider a system of 16 qubits defined on a 4×4 square lattice. This lattice has the square lattice symmetry characterized by $D_4 = \{e, c_4, c_4^2, c_4^3, \sigma_1, \sigma_2, \sigma_3, \sigma_4\}$, where e is an identity operation, c_4 is a rotation operation by $\pi/2$, and σ_i is an inversion operation for each axis as shown in Fig. 3. In the first layer, setting a subgroup $H^{(1)} = D_4$ and a qubit subset $P^{(1)} = \{1, 2, 3\}$ with $\Lambda_1 = 1$, we have a branch of the first layer as $Q_1^{(1)} = \{1, 2, \dots, 16\}$. In the second layer, considering a subset $H^{(2)} = \{e, c_4^2, \sigma_3, \sigma_4\} \leq H^{(1)}$ and the same qubit subset $P^{(2)} = \{1, 2, 3\}$, we obtain the branches of the second layer $Q_1^{(2)}$ and $Q_2^{(2)}$, as shown in Fig. 3. Even in subsequent layers, we can construct the circuit splitting by considering smaller subgroups and

qubit subsets sequentially. Note that the circuit splitting is not unique: a different choice of $\{H_\lambda^{(\ell)}\}$ and $\{P_\lambda^{(\ell)}\}$ results in different circuit splitting. In particular, although this example only considers the case of $\Lambda = 1$ for simplicity, the circuit splitting with $\Lambda > 1$ is allowed.

2. Unitary operators

After determining the circuit splitting at the ℓ th layer, we need to design the unitary operator acting on each branch such that Eq. (7) is satisfied. However, the conventional methods, such as the twirling and nullspace methods, cannot be straightforwardly applied to design the unitary of the equivariant sp-QCNN because its splitting structure acts as a constraint. In other words, the conventional methods consider a single unitary V satisfying $U_g V U_g^\dagger = V$ and do not assume the splitting structure as $\hat{V} = \prod_{\lambda,i} V_{\lambda,i}$ ($V_{\lambda,i}$'s are unitaries acting on different subsets of qubits). Below, we omit the layer index because the unitary operator on each layer can be determined independently.

Our approach to finding unitaries that satisfy Eq. (7)

is to reduce $U_g(\prod_{\lambda,i} V_{\lambda,i})U_g^\dagger = \prod_{\lambda,i} V_{\lambda,i}$ for $g \in G$ to the form of $U_h V_{\lambda,i} U_h^\dagger = V_{\lambda,i}$ for $h \in H$ (H is a subgroup of G), which can be treated with the conventional methods. Suppose that $\mathcal{Q} = \{Q_{\lambda,i}\}$ constructed from $\mathcal{H} = \{H_\lambda\}$ and $\mathcal{P} = \{P_\lambda\}$ by the subgroup method is given for the ℓ th circuit splitting. Let the first coset of H_λ be $C_1^{H_\lambda} = H_\lambda$. In this method, given that the branch $Q_{\lambda,1} = H_\lambda(P_\lambda)$ is invariant under the action of $h \in H_\lambda$ [i.e., $hH_\lambda(P_\lambda) = H_\lambda(P_\lambda)$], we first design $V_{\lambda,1}$ such that

$$U_h V_{\lambda,1} U_h^\dagger = V_{\lambda,1} \quad (37)$$

for $\forall h \in H_\lambda$. Because this condition involves only $V_{\lambda,1}$, the conventional methods, such as the twirling method, can be applied to construct $V_{\lambda,1}$. Once $V_{\lambda,1}$ is constructed using such a method, the other unitaries $V_{\lambda,i}$ ($i \neq 1$) are determined from $V_{\lambda,1}$ through

$$U_{g_i} V_{\lambda,1} U_{g_i}^\dagger = V_{\lambda,i}, \quad (38)$$

where g_i is one of the elements of $C_i^{H_\lambda}$. Then, the unitary operators $V_{\lambda,i}$ constructed in this way satisfy the following relation (see the next paragraph for the proof):

$$U_g \left(\prod_{i=1}^{s_\lambda} V_{\lambda,i} \right) U_g^\dagger = \prod_{i=1}^{s_\lambda} V_{\lambda,i}, \quad (39)$$

for $\forall g \in G$ with $s_\lambda = |G|/|H_\lambda|$. By designing $\prod_{i=1}^{s_\lambda} V_{\lambda,i}$ for each λ in this way, we can construct the G -equivariant convolutional layer V as

$$V = \prod_{\lambda=1}^{\Lambda} \prod_{i=1}^{s_\lambda} V_{\lambda,i}, \quad (40)$$

which satisfies

$$U_g V U_g^\dagger = V \quad (41)$$

for $\forall g \in G$.

We prove Eq. (39) by showing that (i) U_g maps $V_{\lambda,i}$ to another $V_{\lambda,j}$ and that (ii) the map $U_g : \{V_{\lambda,i}\}_i \rightarrow \{V_{\lambda,i}\}_i$ is a bijection. The statement (i) is proved as

$$\begin{aligned} U_g V_{\lambda,i} U_g^\dagger &= U_g U_{g_i} V_{\lambda,1} U_{g_i}^\dagger U_g^\dagger \\ &= U_{gg_i} V_{\lambda,1} U_{gg_i}^\dagger \\ &= U_{g_j h} V_{\lambda,1} U_{g_j h}^\dagger \\ &= U_{g_j} U_h V_{\lambda,1} U_h^\dagger U_{g_j}^\dagger \\ &= U_{g_j} V_{\lambda,1} U_{g_j}^\dagger \\ &= V_{\lambda,j}, \end{aligned} \quad (42)$$

where we have used Eqs. (37)–(38) and $U_{g_1} U_{g_2} = U_{g_1 g_2}$ for $\forall g_1, g_2 \in G$ (because U_g is the representation of G) and defined $gg_i = g_j h$ with $\exists h \in H_\lambda$ and $\exists g_j \in C_j^{H_\lambda}$. In order to prove the statement (ii), it suffices to show that $U_g : \{V_{\lambda,i}\}_i \rightarrow \{V_{\lambda,i}\}_i$ is an injection because $\{V_{\lambda,i}\}_i$ is a finite set. Here, we prove that by contradiction. Assume

that $U_g V_{\lambda,i} U_g^\dagger = U_g V_{\lambda,j} U_g^\dagger$ for $i \neq j$. Then, the assumption readily leads to $V_{\lambda,i} = V_{\lambda,j}$, which contradicts the fact that $V_{\lambda,i}$ and $V_{\lambda,j}$ act on different branches $Q_{\lambda,i}$ and $Q_{\lambda,j}$. Thus, U_g is a bijection. These results mean that U_g just permutes $V_{\lambda,i}$'s, proving Eq. (39), where we have used $[V_{\lambda,i}, V_{\lambda',i'}] = 0$.

We show how to construct unitary operators in Fig. 3 for example. Since the first layer has only one branch, we construct the unitary operator acting on it to satisfy $U_h V_1^{(1)} U_h^\dagger = V_1^{(1)}$ for $\forall h \in H^{(1)}$, which is feasible using the conventional method. In the second layer, we first design $V_1^{(2)}$ acting on $Q_1^{(2)}$ [the left branch in Fig. 3] such that $U_h V_1^{(2)} U_h^\dagger = V_1^{(2)}$ for $\forall h \in H^{(2)}$. Then, we determine $V_2^{(2)}$ as $U_{g_2} V_1^{(2)} U_{g_2}^\dagger = V_2^{(2)}$ with $g_2 \in C_2^{H^{(2)}}$ (say $g_2 = c_4$). Similarly, we can construct the unitary operators after the third layer.

V. DEMONSTRATION: NOISY QUANTUM DATA CLASSIFICATION

In this section, we numerically demonstrate the high measurement efficiency and generalization of equivariant sp-QCNNs in a specific classification task of noisy quantum data.

A. Problem

The equivariant sp-QCNN is suitable for solving problems associated with symmetry. Such problems are often encountered in quantum chemistry, physics, and machine learning, which are the main targets of quantum computing. In practice, when we know the symmetry of quantum states, dynamics, and data distribution of interest in advance, we can exploit the symmetry to improve the accuracy and efficiency of quantum algorithms. Meanwhile, the QCNN excels at capturing correlations of quantum data at various length scales due to its hierarchical structure, which is relevant for quantum many-body systems [28]. Combining these advantages with the splitting structure, the equivariant sp-QCNN improves trainability, generalization, and measurement efficiency compared to conventional QCNNs in various tasks.

We numerically investigate the performance of equivariant sp-QCNNs in the classification task of noisy quantum data. For concreteness, we consider spin models on $2 \times 2 \times 2$ cubic lattice, where spins (or qubits) and their Pauli operators X_j, Y_j , and Z_j are defined on each lattice site. This lattice consists of three types of bonds: A -, B -, and C -bonds as shown in Fig. 4 (a). Here, we consider two types of Heisenberg models, H_1 and H_2 , as

$$H_\mu = \sum_{\langle j,k \rangle} J_{jk}^\mu (X_j X_k + Y_j Y_k + Z_j Z_k) \quad (43)$$

with $\mu = 1, 2$. The summation of $\langle j, k \rangle$ runs over all pairs of nearest neighbor sites j and k . Here, the strength of

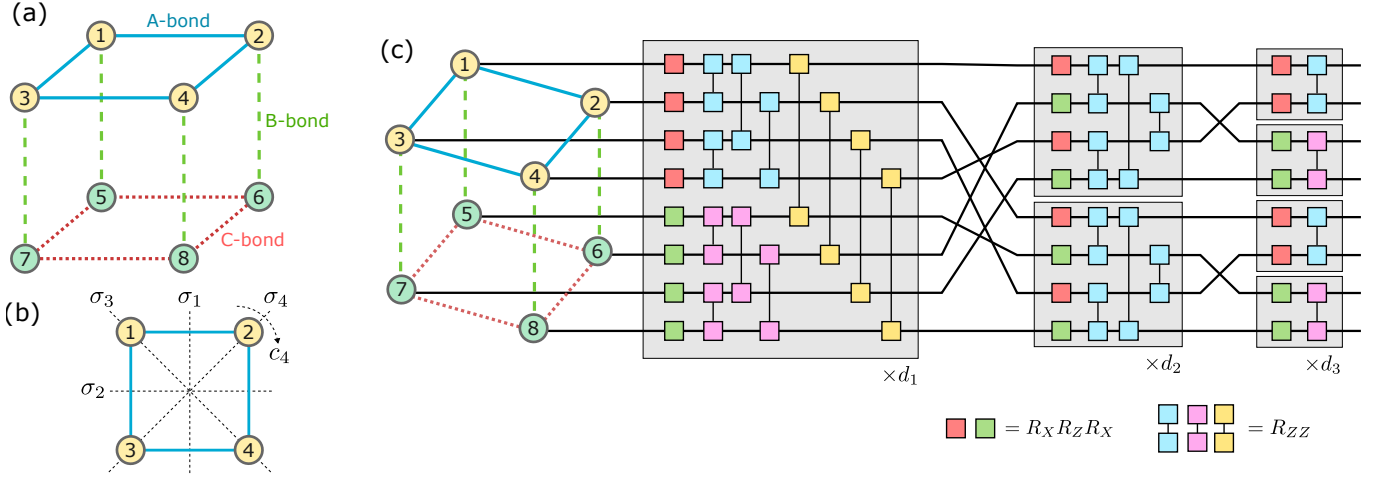


FIG. 4. (a) $2 \times 2 \times 2$ cubic lattice that consists of three types of bonds: A - (blue), B - (green), and C - (red) bonds. (b) This lattice is invariant under the action of $D_4 = \{e, c_4, c_4^2, c_4^3, \sigma_1, \sigma_2, \sigma_3, \sigma_4\}$. (c) The circuit structure of D_4 -equivariant sp-QCNN used in this work. The quantum gates with the same color in each layer indicate that the rotation angles are shared. The details are provided in Appendix B.

exchange interaction J_{jk}^μ depends on the bond types as

$$J_{jk}^\mu = \begin{cases} J_A & \langle j, k \rangle \in A\text{-bond} \\ \pm J_B & \langle j, k \rangle \in B\text{-bond} \\ J_C & \langle j, k \rangle \in C\text{-bond,} \end{cases} \quad (44)$$

where \pm corresponds to $\mu = 1$ and 2 , respectively. Let $|\psi_\mu\rangle$ be the ground state of H_μ . The task here is to classify these two ground states $|\psi_1\rangle$ and $|\psi_2\rangle$.

We assume $|\psi_\mu\rangle$ is disturbed by local noise as

$$|\psi_\mu(\mathbf{n}, \boldsymbol{\epsilon})\rangle = \prod_{j=1}^n e^{i\epsilon_j(n_j^x X_j + n_j^y Y_j + n_j^z Z_j)} |\psi_\mu\rangle, \quad (45)$$

where (n_j^x, n_j^y, n_j^z) is a unit vector uniformly sampled from the two-dimensional unit sphere, and ϵ_j is the rotation angle around (n_j^x, n_j^y, n_j^z) sampled from the normal distribution $\propto \exp(-\epsilon_j^2/2\sigma^2)$ with $\sigma = \gamma\pi/2$ (γ is the noise level). These noisy data cannot be distinguished using any single qubit observable because its expectation value for $|\psi_\mu(\mathbf{n}, \boldsymbol{\epsilon})\rangle$ is zero due to the spin $SU(2)$ symmetry. Let \mathcal{D}_μ be the data distribution for $|\psi_\mu(\mathbf{n}, \boldsymbol{\epsilon})\rangle$.

In this demonstration, we optimize several machine learning models with training data to classify these noisy quantum states and investigate their classification performances. Here, $2N_t$ training data are given by

$$\{|\phi_k\rangle, y_k\}_{k=1}^{2N_t} = \{|\psi_1(\mathbf{n}_k, \boldsymbol{\epsilon}_k)\rangle, y_k = 1\}_{k=1}^{N_t} \sqcup \{|\psi_2(\mathbf{n}_k, \boldsymbol{\epsilon}_k)\rangle, y_k = 0\}_{k=N_t+1}^{2N_t}, \quad (46)$$

where $|\psi_\mu(\mathbf{n}_k, \boldsymbol{\epsilon}_k)\rangle$ is sampled from \mathcal{D}_μ and y_k is the corresponding label ($y_k = 1$ for \mathcal{D}_1 and $y_k = 0$ for \mathcal{D}_2). In this work, we set $J_A = 1.0$, $J_B = 1.5$, $J_C = 1.3$, and $\gamma = 0.4$.

B. Machine learning models

We first clarify the symmetry of the data distribution. From the bond structure of Eq. (44), the Hamiltonian H_μ has the square lattice symmetry characterized by group D_4 :

$$U_g H_\mu U_g^\dagger = H_\mu \quad \forall g \in D_4, \quad (47)$$

$$D_4 = \{e, c_4, c_4^2, c_4^3, \sigma_1, \sigma_2, \sigma_3, \sigma_4\}, \quad (48)$$

where e is an identity operation, c_4 is a rotation operation by $\pi/2$, and σ_i is an inversion operation against each axis. Owing to this symmetry, if the ground state $|\psi_\mu\rangle$ is not degenerate (i.e., it belongs to a one-dimensional irreducible representation of D_4), $|\psi_\mu\rangle$ obeys the following D_4 -symmetry:

$$U_g |\psi_\mu\rangle = c_{g\mu} |\psi_\mu\rangle \quad \forall g \in D_4, \quad (49)$$

where $c_{g\mu} \in \mathbb{C}$ is a phase factor. This symmetry leads to $U_g |\psi_\mu(\mathbf{n}, \boldsymbol{\epsilon})\rangle = c_{g\mu} |\psi_\mu(\mathbf{n}', \boldsymbol{\epsilon}')\rangle$, where $(\mathbf{n}')_j^\mu = n_{g(j)}^\mu$ and $(\boldsymbol{\epsilon}')_j = \epsilon_{g(j)}$. Since the rotation axes \mathbf{n} and angles $\boldsymbol{\epsilon}$ are sampled randomly and independently, the sampling probabilities of $|\psi_\mu(\mathbf{n}, \boldsymbol{\epsilon})\rangle$ and $U_g |\psi_\mu(\mathbf{n}, \boldsymbol{\epsilon})\rangle$ are equivalent:

$$\text{Prob}[|\psi_\mu(\mathbf{n}, \boldsymbol{\epsilon})\rangle \sim \mathcal{D}_\mu] = \text{Prob}[U_g |\psi_\mu(\mathbf{n}, \boldsymbol{\epsilon})\rangle \sim \mathcal{D}_\mu] \quad (50)$$

for $\forall \mathbf{n} \in \mathbb{R}^{3n}, \forall \boldsymbol{\epsilon} \in \mathbb{R}^n, \forall g \in D_4$. In other words, given a quantum data $|\psi\rangle$ sampled from \mathcal{D}_1 or \mathcal{D}_2 , the probability for $|\psi\rangle$ to have been sampled from \mathcal{D}_1 (\mathcal{D}_2) is equal to that for $U_g |\psi\rangle$ to have been sampled from \mathcal{D}_1 (\mathcal{D}_2). Therefore, machine learning models should be designed to satisfy this symmetry condition of Eq. (50).

We consider three types of QCNNS: equivariant and non-equivariant sp-QCNNS and an equivariant randomized QCNN. Figure 4 (c) depicts the unitary circuit of the

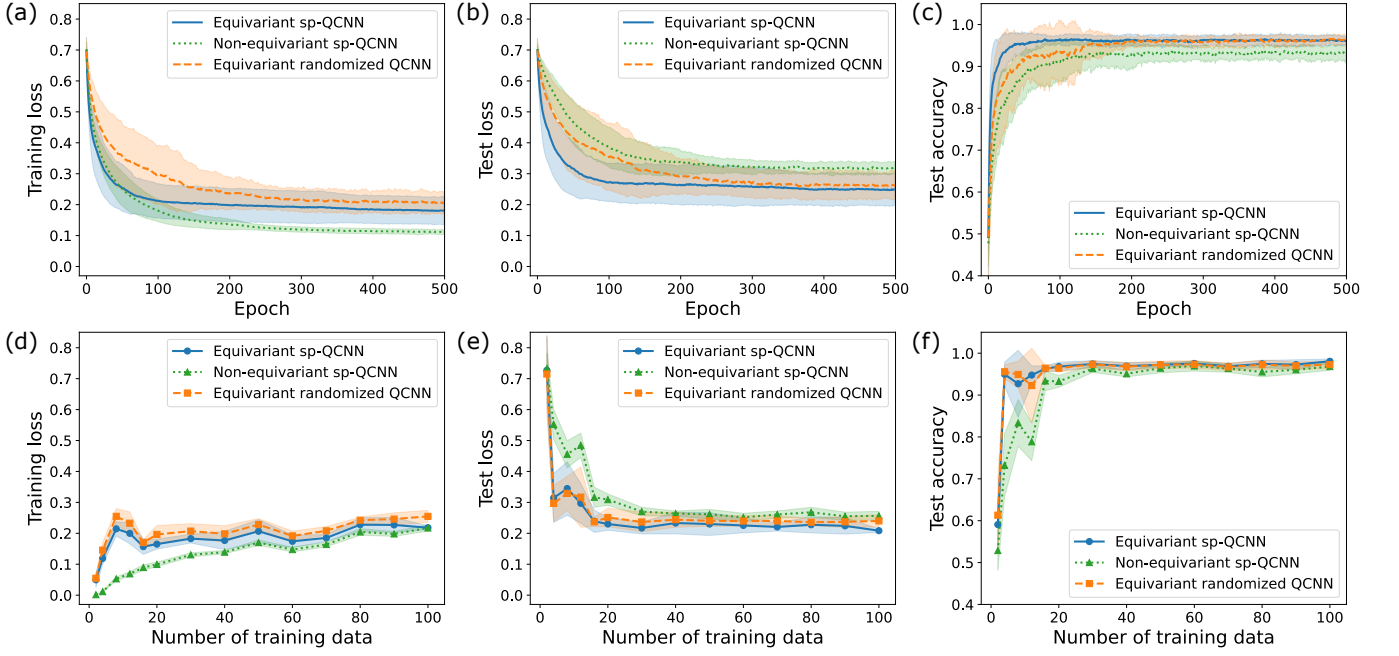


FIG. 5. (a)–(c) Changes in training loss, test loss, and test accuracy during training. The solid, dotted, and dashed lines denote the results for equivariant sp-QCNN, non-equivariant sp-QCNN, and equivariant randomized QCNN, respectively. The shaded areas indicate the standard deviation for the twenty sets of initial parameters. The number of training data is $2N_t = 20$. (d)–(f) Training loss, test loss, and test accuracy after sufficiently long training processes for various numbers of training data. The circles, triangles, and squares denote the results for equivariant sp-QCNN, non-equivariant sp-QCNN, and equivariant randomized QCNN, respectively. The shaded areas indicate the standard deviation for the twenty sets of initial parameters.

equivariant sp-QCNN, which consists of local $R_X R_Z R_X$ and R_{ZZ} rotations (this circuit can be constructed using the subgroup method). In the equivariant sp-QCNN, some rotation gates share the parameter values with other rotation gates to ensure D_4 -equivariance. The non-equivariant sp-QCNN used in this work has the same circuit structure as the equivariant sp-QCNN, but the parameter sharing is not imposed. In the randomized QCNN, one of the eight subcircuits in the equivariant sp-QCNN (corresponding to an output qubit) is randomly chosen for every measurement shot. The unitary circuits $U(\theta)$ of equivariant sp-QCNN and randomized QCNN satisfy D_4 -symmetry as $[U(\theta), U_g] = 0$ for $\forall g \in D_4$. The detailed description of the unitary circuit is provided in Appendix B. In this work, we set the depth of each convolutional layer as $d_1 = d_2 = d_3 = 3$.

We employ logistic regression to classify the noisy data. To this end, after applying $U(\theta)$ to an input state $|\phi\rangle$, we measure the expectation value of a D_4 -symmetric observable $O = \sum_j X_j$ ($[O, U_g] = 0 \forall g \in D_4$), defining the probabilities that ρ belongs to \mathcal{D}_1 and \mathcal{D}_2 as

$$p_1(\theta, |\phi\rangle) = \frac{1}{1 + \exp[-\langle O \rangle]}, \quad (51)$$

$$p_2(\theta, |\phi\rangle) = \frac{1}{1 + \exp[\langle O \rangle]}, \quad (52)$$

with $\langle O \rangle = \langle \phi | U^\dagger(\theta) O U(\theta) | \phi \rangle$. Note that $p_1(\theta, |\phi\rangle)$ and $p_2(\theta, |\phi\rangle)$ satisfy the positivity and the conservation of

probabilities: $p_1(\theta, |\phi\rangle), p_2(\theta, |\phi\rangle) \geq 0$ and $p_1(\theta, |\phi\rangle) + p_2(\theta, |\phi\rangle) = 1$. In the equivariant sp-QCNN and randomized QCNN, the D_4 -symmetry of circuit and observable ensures

$$p_1(\theta, |\phi\rangle) = p_1(\theta, U_g |\phi\rangle), \quad (53)$$

$$p_2(\theta, |\phi\rangle) = p_2(\theta, U_g |\phi\rangle), \quad (54)$$

which can improve the trainability and generalization in the classification task.

To train these QCNN models, we consider the following cross entropy as a loss function:

$$L(\theta) = \frac{1}{2N_t} \sum_{k=1}^{2N_t} [y_k \log p_1(\theta, |\phi_k\rangle) + (1 - y_k) \log p_2(\theta, |\phi_k\rangle)]. \quad (55)$$

We optimize this loss function using the Adam algorithm [47] with the parameter-shift rule. The hyperparameter values used in this work are initial learning rate = 10^{-3} , $\beta_1 = 0.9$, $\beta_2 = 0.999$, and $\eta = 10^{-8}$. We also employ the stochastic gradient descent [48], where only one training data is used to measure the gradient at each iteration.

In this numerical demonstration, we assume that only a few measurement shots are available for the gradient estimation due to limited computational resources. Although the equivariant and non-equivariant sp-QCNNs

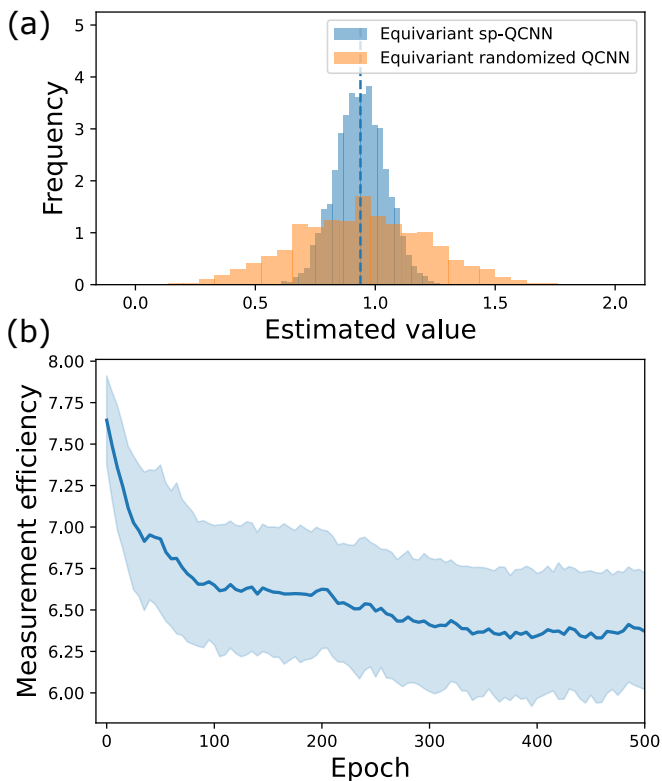


FIG. 6. (a) Histograms for the estimated expectation value of $O = \sum_j X_j$ in the equivariant sp-QCNN and the randomized model. The histograms are computed after 500 epochs. The dashed line is the exact expectation value. We have simulated the quantum circuit with 100 shots 10000 times to obtain the histograms. (b) Change in the measurement efficiency of the equivariant sp-QCNN compared to the randomized model during training. The solid line and shaded area denote the mean and standard deviation for 20 initial parameter sets. The measurement efficiency is defined as the ratio between the variances of the estimated expectation values.

can simultaneously measure the gradient components for different branches as discussed in Sec. III C, we match the total number of measurement shots per iteration for the three models to evaluate the measurement efficiency fairly. The total number of shots for measuring the gradient with the parameter-shift rule is $(2N_{\text{gate}} + 1)N_{\text{shot}}$, where N_{gate} and N_{shot} are the number of rotation gates in the circuit and the number of shots per circuit, respectively. We set $N_{\text{gate}} = 144$ and $N_{\text{shot}} = 5$.

C. Results

The first advantage of the equivariant sp-QCNN is the high generalization performance coming from the equivariance. Figures 5 (a)–(c) show the changes in the training and test losses and the test accuracy during training for the three models. While the non-equivariant sp-QCNN (green dotted lines) achieves the lowest training loss among the three models, its test loss and accuracy

are worse than those of the other models. This indicates that the non-equivariant sp-QCNN is overfitted for the training dataset due to its excessive expressivity. In contrast, the equivariant sp-QCNN and the equivariant randomized model show better test loss and accuracy than the non-equivariant sp-QCNN in Figs. 5 (b) and (c). The high generalization of the equivariant models can also be observed in Figs. 5 (d)–(f), which shows the losses and the accuracy after sufficiently long training processes for various numbers of training data. These results verify that the equivariant models can achieve high test accuracy (or low test loss) with fewer training data than the non-equivariant sp-QCNN. For example, the equivariant models can achieve 90% test accuracy with only 4 training data, whereas the non-equivariant model requires 16 training data for the same accuracy. These results suggest the significance of equivariance, especially when the number of training data is limited.

The second advantage of the equivariant sp-QCNN is the high measurement efficiency stemming from its splitting structure. In Figs. 5 (a)–(c), the equivariant sp-QCNN (blue solid lines) displays faster convergences of training loss, test loss, and test accuracy than the randomized QCNN (orange dashed lines). This result supports the theoretical analysis of the high measurement efficiency of the equivariant sp-QCNNs in Sec. III. In the randomized model, the large statistical errors of the gradient estimation disturb the stable and fast optimization to slow down the training process. Conversely, the high measurement efficiency of the equivariant sp-QCNN suppresses the statistical errors to stabilize the optimization and accelerate the training process.

Finally, we quantify the measurement efficiency of the equivariant sp-QCNN. In quantum computing, statistical errors in estimating expectation values are inevitable due to finite measurement resources. The equivariant sp-QCNN can suppress the statistical errors compared to the randomized model because the splitting structure enables us to obtain n times more measurement outcomes. In general, the variance of the estimated expectation value decays as $\mathcal{O}(1/N_{\text{shot}})$ according to the central limit theorem. Therefore, we here define the relative measurement efficiency as $r = v_{\text{rand}}/v_{\text{sp}}$, where v_{sp} and v_{rand} are the variances of the estimated expectation values in the equivariant sp-QCNN and the randomized model, respectively [see Fig. 6 (a) for example]. This quantification indicates that the equivariant sp-QCNN can achieve the same accuracy as the randomized model only with $1/r$ times fewer measurement shots. Figure 6 (b) shows the change in the relative measurement efficiency during training [the hyperparameters are the same as those used in Figs. 5(a)–(c)]. We observe that the measurement efficiency remains high during training: it begins at about 7.7 and converges to 6.3. That is, the equivariant sp-QCNN can ideally reduce the required measurement shots by at least $1/6.3$ times in this problem. Note that this calculation of $n = 8$ alone is not sufficient to prove that the equivariant sp-QCNN can improve

the measurement efficiency by a factor of $\mathcal{O}(n)$. Nevertheless, a previous study numerically verified the $\mathcal{O}(n)$ times improvement for a translationally equivariant sp-QCNN [33], suggesting that, with our numerical results, similar improvements are available even for other symmetries.

VI. CONCLUSIONS

In this work, we have proposed an improved framework for QCNNs, equivariant sp-QCNNs, which integrates the circuit splitting structure with the equivariance for general symmetries. The equivariant sp-QCNN splits the quantum circuit instead of discarding the qubits in the pooling layer, being a resource-efficient model of equivariant QCNNs with high trainability and generalization performance. By maximally leveraging the qubit resource, the equivariant sp-QCNN ideally improves the measurement efficiency by a factor of $\mathcal{O}(n)$ compared to the conventional equivariant QCNN. Furthermore, the splitting structure never spoils the high trainability of QCNNs. We have introduced a group-theoretical method of constructing equivariant sp-QCNNs, establishing the basis for general model design. The numerical experiment for the specific classification task has demonstrated that our model outperforms the conventional equivariant and non-equivariant QCNNs in terms of the resources required for training, highlighting the effectiveness of the equivariant sp-QCNN.

We mention some future research directions on equivariant sp-QCNNs. The first one is the investigation of classical simulability. A critical conjecture on QNNs has recently been raised, stating that provably barren plateau-free models are classically simulable [49]. This conjecture may prevent the exponential quantum advantages of many QNN models, including QCNNs. However, Ref. [49] also mentions a loophole in this conjecture for QCNNs: QCNNs may become classically non-simulable after some training, even if they are classically simulable at the beginning of training where the parameters are randomly initialized. Therefore, investigating whether QCNNs (and sp-QCNNs) after training are classically simulable for specific tasks is a significant research direction toward practical quantum advantages beyond classical simulations. Second, applying equivariant sp-QCNNs to quantum many-body problems is an intriguing direction. It is known that the conventional QCNN has a similar structure to the multiscale entanglement renormalization ansatz (MERA), a representative tensor network model describing one-dimensional critical quantum systems [50]. On the other hand, the sp-QCNN has a similar structure to the branching MERA, which is known as a good ansatz for describing higher-dimensional quantum critical systems [51]. Thus, the sp-QCNN may be suitable for representing higher dimensional critical phenomena in various quantum algorithms, such as variational quantum eigensolvers [6].

ACKNOWLEDGMENTS

Fruitful discussions with Yuichi Kamata and Nasa Matsumoto are gratefully acknowledged. The numerical simulations in this work use Qulacs, an open-source quantum circuit simulator [52].

Appendix A: Details of circuit splitting

In this Appendix, we provide the details of circuit splitting in the subgroup method.

1. Sufficient conditions for circuit splitting

This section provides sufficient conditions for appropriate circuit splitting, which forms the basis for the subgroup method. Before moving on to the details, we summarize the requirements for the G -equivariant circuit splitting $\mathcal{Q}^{(\ell)} = \{Q_i^{(\ell)}\}_i$ as follows:

1. G -invariance:

$$g(Q^{(\ell)}) = \mathcal{Q}^{(\ell)} \text{ for } \forall g \in G. \quad (\text{A1})$$

2. Branches do not merge:

$$\forall i, \exists j \text{ s.t. } Q_i^{(\ell+1)} \subseteq Q_j^{(\ell)}. \quad (\text{A2})$$

3. Branches are a partition of qubits $Q_{\text{bit}} = [n]$:

$$Q_i^{(\ell)} \cap Q_j^{(\ell)} = \emptyset \text{ for } i \neq j, \quad (\text{A3})$$

$$\bigcup_i Q_i^{(\ell)} = Q_{\text{bit}}. \quad (\text{A4})$$

In what follows, we provide sufficient conditions for these three requirements one by one.

For convenience, we recall the following terms regarding the action of G on Q_{bit} .

Definition 1 (G -equivalence of qubits). We say that qubits $q_1, q_2 \in Q_{\text{bit}}$ are G -equivalent and denote $q_1 \sim q_2$ if and only if there exists $g \in G$ such that $g(q_1) = q_2$.

Definition 2 (G -independence of qubits). We say that a subset of qubits $Q_1 \subseteq Q_{\text{bit}}$ is G -independent if and only if $\forall q_1, q_2 \in Q_1$ ($q_1 \neq q_2$) are not G -equivalent.

Definition 3 (G -completeness of qubits). We say that a subset of qubits $Q_1 \subseteq Q_{\text{bit}}$ is G -complete if and only if, for any $q \in Q_{\text{bit}}$, there exists $q_1 \in Q_1$ that is G -equivalent to q .

a. *Sufficient condition for G-invariance*

Here, we show that the subgroup method introduced in the main text ensures the G -invariance of Eq. (A1). To this end, we first prove the following theorem, which is the core of this method.

Theorem 1. *Let H be a subgroup of G and P a subset of Q_{bit} . Given the coset decomposition $G = \bigsqcup_{i=1}^s C_i^H$, we define*

$$Q_i = C_i^H(P) = \{g(q) \mid g \in C_i^H, q \in P\}. \quad (\text{A5})$$

Then, $\mathcal{Q} = \{Q_i\}_{i \in [s]}$ is G -invariant.

Proof. We prove this theorem by showing that (i) $g \in G$ maps $Q_i \in \mathcal{Q}$ to another $Q_j \in \mathcal{Q}$ [i.e., $g(Q_i) = Q_j$] and that (ii) the map $g: \mathcal{Q} \rightarrow \mathcal{Q}$ is a bijection.

First, we prove the statement (i). According to the group theory, the action of $g \in G$ changes a coset C_i^H to another coset C_j^H , namely $gC_i^H = C_j^H$. Using this property, we can show the statement (i) as

$$g(Q_i) = gC_i^H(P) = C_j^H(P) = Q_j. \quad (\text{A6})$$

Next, we prove the statement (ii). Because \mathcal{Q} is a finite set, it suffices to show that the map g is an injection. We here give the proof by contradiction. Assume $g(Q_i) = g(Q_j)$ for $Q_i \neq Q_j$. Then, multiplying g^{-1} on both sides, we have $Q_i = Q_j$, which contradicts $Q_i \neq Q_j$ in the assumption. This shows that $g(Q_i) \neq g(Q_j)$ for $Q_i \neq Q_j$, proving that the map g is an injection and thus a bijection. \square

This theorem proves the following corollary, which shows that the circuit splitting constructed by the subgroup method is guaranteed to be G -invariant.

Corollary 1. *Let H_λ be a subgroup of G and P_λ a subset of Q_{bit} ($\lambda = 1, \dots, \Lambda$). Given the coset decompositions $G = \bigsqcup_{i=1}^{s_\lambda} C_i^{H_\lambda}$, we define*

$$Q_{\lambda,i} = C_i^{H_\lambda}(P_\lambda) = \{g(q) \mid g \in C_i^{H_\lambda}, q \in P_\lambda\}. \quad (\text{A7})$$

Then, $\mathcal{Q} = \{Q_{\lambda,i}\}_{\lambda \in [\Lambda], i \in [s_\lambda]}$ is G -invariant.

Proof. We consider subsets of \mathcal{Q} as follows:

$$\mathcal{S}_\lambda \equiv \{Q_{\lambda,i}\}_{i \in [s_\lambda]}, \quad (\text{A8})$$

where $\mathcal{Q} = \bigcup_\lambda \mathcal{S}_\lambda$. According to Theorem 1, \mathcal{S}_λ is G -invariant. Therefore, the union of \mathcal{S}_λ , namely \mathcal{Q} , is also G -invariant. \square

b. *Sufficient condition for branches not to merge*

Here, we give a sufficient condition for branches not to merge in the pooling layer [Eq. (A2)].

Theorem 2. *Let $\mathcal{Q}^{(\ell)} = \{Q_{\lambda,i}^{(\ell)}\}$ be G -invariant branches constructed by the subgroup method with subgroups $\{H_\lambda^{(\ell)}\}$ and qubit subsets $\{P_\lambda^{(\ell)}\}$. If, for $\forall \lambda$, there exists λ' such that*

$$H_\lambda^{(\ell+1)} \leq H_{\lambda'}^{(\ell)}, \quad P_\lambda^{(\ell+1)} \subseteq P_{\lambda'}^{(\ell)}, \quad (\text{A9})$$

then $\mathcal{Q}^{(\ell)}$ and $\mathcal{Q}^{(\ell+1)}$ satisfy Eq. (A2), i.e., the branches do not merge in the pooling layer.

Proof. According to the group theory, if $H_\lambda^{(\ell+1)} \leq H_{\lambda'}^{(\ell)}$, any coset of $H_\lambda^{(\ell+1)}$ is included in a corresponding coset of $H_{\lambda'}^{(\ell)}$ as

$$\forall i, \exists j \text{ s.t. } C_i^{H_\lambda^{(\ell+1)}} \subseteq C_j^{H_{\lambda'}^{(\ell)}}, \quad (\text{A10})$$

where $C_i^{H_\lambda^{(\ell+1)}}$ and $C_j^{H_{\lambda'}^{(\ell)}}$ are cosets of $H_\lambda^{(\ell+1)}$ and $H_{\lambda'}^{(\ell)}$, respectively. This leads to an inclusion relation as

$$\begin{aligned} Q_{\lambda,i}^{(\ell+1)} &= C_i^{H_\lambda^{(\ell+1)}}(P_\lambda^{(\ell+1)}) \\ &\subseteq C_j^{H_{\lambda'}^{(\ell)}}(P_\lambda^{(\ell+1)}) \\ &\subseteq C_j^{H_{\lambda'}^{(\ell)}}(P_{\lambda'}^{(\ell)}) \\ &= Q_{\lambda',j}^{(\ell)}, \end{aligned} \quad (\text{A11})$$

where we have used $C_i^{H_\lambda^{(\ell+1)}} \subseteq C_j^{H_{\lambda'}^{(\ell)}}$ in the second line and $P_\lambda^{(\ell+1)} \subseteq P_{\lambda'}^{(\ell)}$ in the third line. This proves Eq (A2). \square

c. *Sufficient condition for branches to be a partition of qubits*

Here, we prove the following Theorem, providing a sufficient condition for branches to be a partition of qubits [Eqs. (A3) and (A4)]:

Theorem 3. *Consider branches $\{Q_{\lambda,i}\}$ defined by $\mathcal{H} = \{H_\lambda\}$ and $\mathcal{P} = \{P_\lambda\}$. Then, the following conditions are sufficient for branches to be a partition of qubits, i.e., to satisfy Eqs. (A3) and (A4):*

$$(i) \quad |G(q)|/|H_\lambda(q)| = s_\lambda \text{ for } \forall q \in P_\lambda,$$

$$(ii) \quad \bigsqcup_\lambda P_\lambda \text{ is } G\text{-independent,}$$

$$(iii) \quad \bigsqcup_\lambda P_\lambda \text{ is } G\text{-complete,}$$

where $s_\lambda = |G|/|H_\lambda|$ is the number of independent cosets.

Proof. We first prove that conditions (i) and (ii) are sufficient for Eq. (A3). By condition (ii), we have $G(P_\lambda) \cap G(P_{\lambda'}) = \emptyset$ for $\lambda \neq \lambda'$. This leads to $Q_{\lambda,i} \cap Q_{\lambda',i'} = \emptyset$ for $\lambda \neq \lambda'$, where we have used $Q_{\lambda,i} \subseteq G(P_\lambda)$ and $Q_{\lambda',i'} \subseteq G(P_{\lambda'})$. Thus, it suffices to prove $Q_{\lambda,i} \cap Q_{\lambda,i'} = \emptyset$ for $i \neq i'$.

We prove this by contradiction. Assume that there exist $i \neq i'$ such that $Q_{\lambda,i} \cap Q_{\lambda,i'} \neq \emptyset$. By definition of coset decomposition $G = \bigsqcup_{i=1}^{s_\lambda} C_i^{H_\lambda}$, we have

$$G(P_\lambda) = \{g(q) \mid g \in G, q \in P_\lambda\} \quad (\text{A12})$$

$$= \bigcup_{i=1}^{s_\lambda} \{g(q) \mid g \in C_i^{H_\lambda}, q \in P_\lambda\} \quad (\text{A13})$$

$$= \bigcup_{i=1}^{s_\lambda} Q_{\lambda,i}. \quad (\text{A14})$$

Taking the norm on the leftmost and rightmost sides, the following inequality holds:

$$|G(P_\lambda)| = \left| \bigcup_{i=1}^{s_\lambda} Q_{\lambda,i} \right| < \sum_{i=1}^{s_\lambda} |Q_{\lambda,i}|, \quad (\text{A15})$$

where we have used that assumption that $Q_{\lambda,i} \cap Q_{\lambda,i'} \neq \emptyset$ for some $i \neq i'$. Because of $|Q_{\lambda,i}| = |g_i H_\lambda(P_\lambda)| = |H_\lambda(P_\lambda)|$, the above inequality is reduced to

$$|G(P_\lambda)| < s_\lambda |H_\lambda(P_\lambda)|. \quad (\text{A16})$$

Given that P_λ is G -independent by condition (ii), we have

$$|G(P_\lambda)| = \sum_{q \in P_\lambda} |G(q)|, \quad (\text{A17})$$

$$|H_\lambda(P_\lambda)| = \sum_{q \in P_\lambda} |H_\lambda(q)|, \quad (\text{A18})$$

and thus

$$\sum_{q \in P_\lambda} |G(q)| < s_\lambda \sum_{q \in P_\lambda} |H_\lambda(q)|. \quad (\text{A19})$$

This contradicts condition (i), i.e., $|G(q)|/|H_\lambda(q)| = s_\lambda$ for all $q \in P_\lambda$. Therefore, the assumption that there exist $i \neq i'$ such that $Q_{\lambda,i} \cap Q_{\lambda,i'} \neq \emptyset$ is incorrect, and conditions (i) and (ii) are sufficient for Eq. (A3).

We finally prove that condition (iii) leads to Eq. (A4). From Eq. (A14), we have $\bigcup_{\lambda,i} Q_{\lambda,i} = \bigcup_\lambda G(P_\lambda)$. By condition (iii), we also have $\bigcup_\lambda G(P_\lambda) = Q_{\text{bit}}$, thereby obtaining $\bigcup_{\lambda,i} Q_{\lambda,i} = Q_{\text{bit}}$. This proves that condition (iii) is sufficient for Eq. (A4). \square

Below, we say that a qubit $q \in Q_{\text{bit}}$ is *well-behaved* for a subgroup H if $|G(q)|/|H(q)| = |G|/|H| = s$ holds. Note that confirming whether a qubit $q \in Q_{\text{bit}}$ is well-behaved is easy unless $|G|$ is too large to track all elements of $G(q)$.

2. Systematic method of circuit splitting

We are ready to present a systematic method of finding the circuit splitting that satisfies Eqs. (A1)–(A4). By Corollary 1, the subgroup method allows us to obtain the G -invariant branches $\mathcal{Q}^{(\ell)} = \{Q_{\lambda,i}^{(\ell)}\}$ based on subgroups

$\mathcal{H}^{(\ell)} = \{H_\lambda^{(\ell)}\}$ and qubit subsets $\mathcal{P}^{(\ell)} = \{P_\lambda^{(\ell)}\}$. In addition to the G -invariance, the branches $\mathcal{Q}^{(\ell)}$ must satisfy Eqs. (A2)–(A4). According to Theorems 2 and 3, the following conditions are sufficient:

$$1. \forall \lambda, \exists \lambda' \text{ s.t. } H_\lambda^{(\ell+1)} \leq H_{\lambda'}^{(\ell)} \text{ and } P_\lambda^{(\ell+1)} \subseteq P_{\lambda'}^{(\ell)}, \quad (\text{A20})$$

$$2. |G(q)|/|H_\lambda^{(\ell)}(q)| = s_\lambda^{(\ell)} \text{ for } \forall q \in P_\lambda^{(\ell)}, \quad (\text{A21})$$

$$3. \bigsqcup_\lambda P_\lambda \text{ is } G\text{-independent and } G\text{-complete}, \quad (\text{A22})$$

where $s_\lambda^{(\ell)} = |G|/|H_\lambda^{(\ell)}|$.

In order to find $\mathcal{H}^{(\ell)}$ and $\mathcal{P}^{(\ell)}$ satisfying these conditions, we employ a brute-force method. This method begins with considering all subgroups of G and corresponding well-behaved qubits. For instance, Fig. 7 shows all subgroups of $G = D_4$ for a 4×4 qubits array. The qubit $q \in Q_{\text{bit}}$ represented by a colored (not white) box is well-behaved for the corresponding subgroup H . The same colored (red, yellow, or blue) boxes, say $q_1, q_2 \in Q_{\text{bit}}$, denote G -equivalent qubits that are mapped to each other by an action of $g \in G$ as $g(q_1) = q_2$. Obtaining this diagram requires only a polynomial computational cost in the number of qubits n and is thus practically possible unless $|G|$ is so large that all subgroups are not available.

Based on this diagram, we first set subgroups and qubit subsets of the final layer $\{(H_\lambda^{(L)}, P_\lambda^{(L)})\}_\lambda$. We choose them such that

$$\bigsqcup_\lambda P_\lambda^{(L)} \text{ contains one qubit of each color.}$$

The final layer constructed in this way, where $\bigsqcup_\lambda P_\lambda^{(L)}$ contains only colored (i.e., well-behaved) qubits and their colors are complete and not duplicated, necessarily satisfies Eqs. (A21) and (A22). For example, in Fig. 7, we can choose the qubits marked by the red stars as $P = \{1, 2, 3\}$ with $H = \{e, \sigma_3\}$, reproducing the third layer in Fig. 3.

After determining $\{(H_\lambda^{(L)}, P_\lambda^{(L)})\}_\lambda$ of the final layer, we set $\{(H_\lambda^{(\ell)}, P_\lambda^{(\ell)})\}_\lambda$ layer by layer from $\ell = L$ to $\ell = 1$. Then, we are allowed to perform the following operations on $\{(H_\lambda^{(\ell)}, P_\lambda^{(\ell)})\}_\lambda$:

1. Merge two qubit subsets P_1 and P_2 if their accompanying subgroups are the same:

$$(H, P_1), (H, P_2) \rightarrow (H, P_1 \sqcup P_2). \quad (\text{A23})$$

2. Change a subgroup H_1 to a larger one H_2 (i.e., $H_1 \leq H_2$):

$$(H_1, P) \rightarrow (H_2, P). \quad (\text{A24})$$

We can perform these operations repeatedly to construct the ℓ th circuit splitting from the $(\ell + 1)$ th one. This construction trivially satisfies Eq. (A20) and thus Eq. (A2). Furthermore, Eqs. (A21) and (A22) hold even after the above two operations. This is because $\bigsqcup_\lambda P_\lambda$ remains unchanged in these operations for Eq. (A22), and the following lemma explains Eq. (A21):

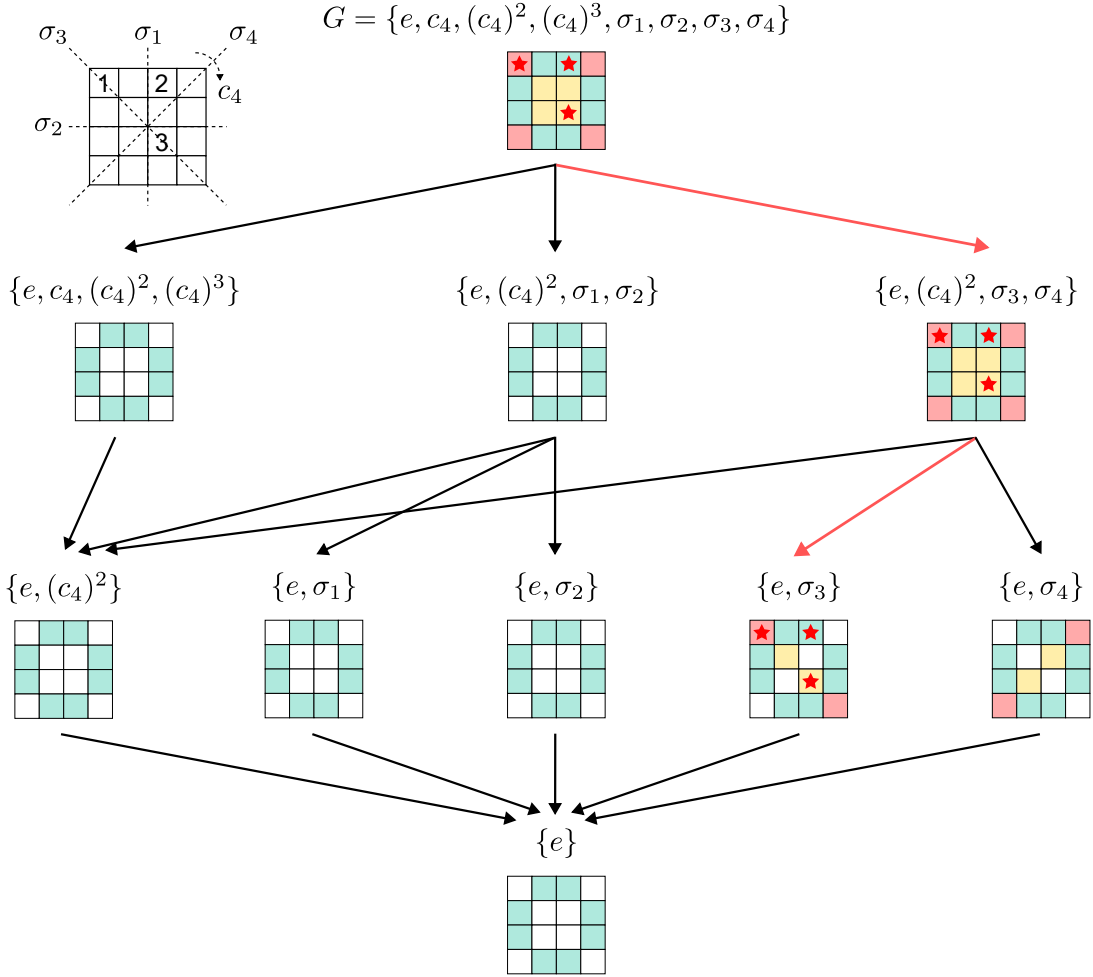


FIG. 7. All subgroups of D_4 and well-behaved qubits on the 4×4 lattice. The qubit represented by a colored (not white) box is well-behaved for the corresponding subgroup. The same colored (red, yellow, or blue) boxes denote G -equivalent qubits. We can reproduce the circuit splitting of Fig. 3 by choosing the subgroups and qubit subsets marked by the red stars.

Lemma 1. Let H_1 and H_2 be subgroups of G satisfying $H_1 \leq H_2$. For $q \in Q_{bit}$, if $|G(q)|/|H_1(q)| = s_1$ holds, then $|G(q)|/|H_2(q)| = s_2$ also holds, where we have defined $s_1 = |G|/|H_1|$ and $s_2 = |G|/|H_2|$.

Proof. Given that H_1 is a subgroup of H_2 , any coset of H_2 is a disjoint union of cosets of H_1 as

$$C_i^{H_2} = \bigsqcup_{j \in \sigma_i} C_j^{H_1} \quad (\text{A25})$$

with $\sigma_i \subseteq [s_2]$ ($|\sigma_i| = |H_2|/|H_1|$). Meanwhile, by Theorem 3, $|G(q)|/|H_1(q)| = s_1$ leads to

$$G(q) = C_1^{H_1}(q) \sqcup \dots \sqcup C_{s_1}^{H_1}(q), \quad (\text{A26})$$

where $C_i^{H_1}(q) \cap C_j^{H_1}(q) = \emptyset$ holds for $i \neq j$. Combining Eqs. (A25) and (A26), we have

$$G(q) = C_1^{H_2}(q) \sqcup \dots \sqcup C_{s_2}^{H_2}(q), \quad (\text{A27})$$

where $C_i^{H_2}(q) \cap C_j^{H_2}(q) = \emptyset$ for $i \neq j$. Since $|C_i^{H_2}(q)| = |H_2(q)|$ for all i , we obtain $|G(q)| = s_2|H_2(q)|$. \square

In Fig. 7, we can construct earlier layers by modifying the subgroup as $H = \{e, \sigma_3\} \rightarrow \{e, (c_4)^2, \sigma_3, \sigma_4\} \rightarrow D_4$ with $P = \{1, 2, 3\}$ being fixed. This reproduces the second and the first layers in Fig. 3.

Appendix B: Unitary circuit of numerical experiment

Here, we describe the details of the unitary circuit in the numerical experiment. For convenience, we assign each qubit a number from one to eight, as shown in Fig. 4. The unitary circuit of the equivariant sp-QCNN has three convolutional (or fully-connected) layers as

$$U(\boldsymbol{\theta}) = V^{(3)}(\boldsymbol{\theta}^{(3)})V^{(2)}(\boldsymbol{\theta}^{(2)})V^{(1)}(\boldsymbol{\theta}^{(1)}). \quad (\text{B1})$$

Each convolutional layer consists of multiple branches:

$$Q_1^{(1)} = \{1, 2, 3, 4, 5, 6, 7, 8\}, \quad (\text{B2})$$

$$Q_1^{(2)} = \{1, 4, 6, 7\}, \quad (\text{B3})$$

$$Q_2^{(2)} = \{2, 3, 5, 8\}, \quad (\text{B4})$$

$$Q_1^{(3)} = \{1, 4\}, \quad (\text{B5})$$

$$Q_2^{(3)} = \{6, 7\}, \quad (\text{B6})$$

$$Q_3^{(3)} = \{2, 3\}, \quad (\text{B7})$$

$$Q_4^{(3)} = \{5, 8\}. \quad (\text{B8})$$

The first convolutional layer $V^{(1)} = V_1^{(1)}$ is given by

$$\begin{aligned} V_1^{(1)}(\boldsymbol{\theta}) &= \prod_{i=1}^{d_1} \left(\left(\prod_{\langle j,k \rangle \in Q_1^{(1)}} R_{j,k}(\delta_{j,k}^i) \right) \left(\prod_{j \in Q_1^{(1)}} R_j(\alpha_j^i) \right) \right), \end{aligned} \quad (\text{B9})$$

where we have defined

$$R_j(\boldsymbol{\alpha}) = R_{X_j}(\alpha_1) R_{Z_j}(\alpha_2) R_{X_j}(\alpha_3), \quad (\text{B10})$$

$$R_{j,k}(\delta) = R_{Z_j Z_k}(\delta). \quad (\text{B11})$$

The $\langle j, k \rangle$ denotes the nearest neighbor qubit pair on the $2 \times 2 \times 2$ cubic lattice. To ensure the equivariance, some rotation gates share the parameter values with other rotation gates as

$$\delta_{1,2}^i = \delta_{2,4}^i = \delta_{4,3}^i = \delta_{3,1}^i, \quad (\text{B12})$$

$$\delta_{5,6}^i = \delta_{6,8}^i = \delta_{8,7}^i = \delta_{7,5}^i, \quad (\text{B13})$$

$$\delta_{1,5}^i = \delta_{2,6}^i = \delta_{3,7}^i = \delta_{4,8}^i, \quad (\text{B14})$$

$$\alpha_1^i = \alpha_2^i = \alpha_3^i = \alpha_4^i, \quad (\text{B15})$$

$$\alpha_5^i = \alpha_6^i = \alpha_7^i = \alpha_8^i. \quad (\text{B16})$$

The second convolutional layer $V^{(2)} = V_2^{(2)} V_1^{(2)}$ is given by

$$\begin{aligned} V_1^{(2)}(\boldsymbol{\theta}) &= \prod_{i=1}^{d_2} \left(\left(\prod_{\langle j,k \rangle \in P_2} R_{j,k}(\delta_{j,k}^i) \right) \left(\prod_{j \in Q_1^{(2)}} R_j(\alpha_j^i) \right) \right), \end{aligned} \quad (\text{B17})$$

$$V_2^{(2)}(\boldsymbol{\theta}) = U_{c_4} V_1^{(2)}(\boldsymbol{\theta}) U_{c_4}^\dagger, \quad (\text{B18})$$

where we have defined $P_2 = \{(1, 6), (6, 4), (4, 7), (7, 1)\}$. The parameters are shared as

$$\delta_{1,6}^i = \delta_{6,4}^i = \delta_{4,7}^i = \delta_{7,1}^i, \quad (\text{B19})$$

$$\alpha_1^i = \alpha_4^i, \quad (\text{B20})$$

$$\alpha_6^i = \alpha_7^i. \quad (\text{B21})$$

The third convolutional (or fully-connected) layer $V^{(3)} = V_4^{(3)} V_3^{(3)} V_2^{(3)} V_1^{(3)}$ is given by

$$V_1^{(3)}(\boldsymbol{\theta}) = \prod_{i=1}^{d_3} R_{1,4}(\delta_{1,4}^i) R_1(\alpha_1^i) R_4(\alpha_4^i), \quad (\text{B22})$$

$$V_2^{(3)}(\boldsymbol{\theta}) = \prod_{i=1}^{d_3} R_{6,7}(\delta_{6,7}^i) R_6(\alpha_6^i) R_7(\alpha_7^i), \quad (\text{B23})$$

$$V_3^{(3)}(\boldsymbol{\theta}) = U_{c_4} V_1^{(3)}(\boldsymbol{\theta}) U_{c_4}^\dagger, \quad (\text{B24})$$

$$V_4^{(3)}(\boldsymbol{\theta}) = U_{c_4} V_2^{(3)}(\boldsymbol{\theta}) U_{c_4}^\dagger, \quad (\text{B25})$$

with parameter sharing

$$\alpha_1^i = \alpha_4^i, \quad (\text{B26})$$

$$\alpha_6^i = \alpha_7^i. \quad (\text{B27})$$

-
- [1] P. W. Shor, Polynomial-Time Algorithms for Prime Factorization and Discrete Logarithms on a Quantum Computer, *SIAM J. Comput.* **26**, 1484–1509 (1997).
- [2] L. K. Grover, Quantum mechanics helps in searching for a needle in a haystack, *Phys. Rev. Lett.* **79**, 325 (1997).
- [3] C. Gidney and M. Ekerå, How to factor 2048 bit RSA integers in 8 hours using 20 million noisy qubits, *Quantum* **5**, 433 (2021), 1905.09749v3.
- [4] J. Preskill, Quantum computing in the NISQ era and beyond, *Quantum* **2**, 79 (2018).
- [5] M. Cerezo, A. Arrasmith, R. Babbush, S. C. Benjamin, S. Endo, K. Fujii, J. R. McClean, K. Mitarai, X. Yuan, L. Cincio, and P. J. Coles, Variational quantum algorithms, *Nat. Rev. Phys.* **3**, 625 (2021).
- [6] A. Peruzzo, J. McClean, P. Shadbolt, M.-H. Yung, X.-Q. Zhou, P. J. Love, A. Aspuru-Guzik, and J. L. O’Brien, A variational eigenvalue solver on a photonic quantum processor, *Nat. Commun.* **5**, 4213 (2014).
- [7] E. Farhi and H. Neven, Classification with quantum neural networks on near term processors, *arXiv:1802.06002 [quant-ph]* (2018).
- [8] K. Mitarai, M. Negoro, M. Kitagawa, and K. Fujii, Quantum circuit learning, *Phys. Rev. A* **98**, 032309 (2018).
- [9] M. Benedetti, E. Lloyd, S. Sack, and M. Fiorentini, Parameterized quantum circuits as machine learning models, *Quantum Sci. Technol.* **4**, 043001 (2019).
- [10] M. Schuld, A. Bocharov, K. M. Svore, and N. Wiebe, Circuit-centric quantum classifiers, *Phys. Rev. A* **101**, 032308 (2020).
- [11] E. Farhi, J. Goldstone, and S. Gutmann, A quantum approximate optimization algorithm, *arXiv:1411.4028 [quant-ph]* (2014).

- [12] J. R. McClean, S. Boixo, V. N. Smelyanskiy, R. Babbush, and H. Neven, Barren plateaus in quantum neural network training landscapes, *Nat. Commun.* **9**, 4812 (2018).
- [13] M. Cerezo, A. Sone, T. Volkoff, L. Cincio, and P. J. Coles, Cost function dependent barren plateaus in shallow parametrized quantum circuits, *Nat. Commun.* **12**, 1791 (2021).
- [14] C. Ortiz Marrero, M. Kieferová, and N. Wiebe, Entanglement-induced barren plateaus, *PRX quantum* **2**, 040316 (2021).
- [15] Z. Holmes, K. Sharma, M. Cerezo, and P. J. Coles, Connecting ansatz expressibility to gradient magnitudes and barren plateaus, *PRX quantum* **3**, 010313 (2022).
- [16] M. Larocca, S. Thanasilp, S. Wang, K. Sharma, J. Biamonte, P. J. Coles, L. Cincio, J. R. McClean, Z. Holmes, and M. Cerezo, A Review of Barren Plateaus in Variational Quantum Computing, [arXiv:2405.00781 \[quant-ph\]](https://arxiv.org/abs/2405.00781) (2024).
- [17] M. M. Bronstein, J. Bruna, T. Cohen, and P. Veličković, Geometric deep learning: Grids, groups, graphs, geodesics, and gauges, [arXiv:2104.13478 \[cs.LG\]](https://arxiv.org/abs/2104.13478) (2021).
- [18] G. Verdon, T. McCourt, E. Luzhnica, V. Singh, S. Leichenauer, and J. Hidary, Quantum Graph Neural Networks, [arXiv:1909.12264 \[quant-ph\]](https://arxiv.org/abs/1909.12264) (2019).
- [19] H. Zheng, Z. Li, J. Liu, S. Strelchuk, and R. Kondor, Speeding up learning quantum states through group equivariant convolutional quantum ansätze, *PRX quantum* **4**, 020327 (2023).
- [20] M. Larocca, F. Sauvage, F. M. Sbahi, G. Verdon, P. J. Coles, and M. Cerezo, Group-invariant quantum machine learning, *PRX quantum* **3**, 030341 (2022).
- [21] J. J. Meyer, M. Mularski, E. Gil-Fuster, A. A. Mele, F. Arzani, A. Wilms, and J. Eisert, Exploiting symmetry in variational quantum machine learning, *PRX quantum* **4**, 010328 (2023).
- [22] A. Skolik, M. Cattelan, S. Yarkoni, T. Bäck, and V. Dunjko, Equivariant quantum circuits for learning on weighted graphs, [arXiv:2205.06109 \[quant-ph\]](https://arxiv.org/abs/2205.06109) (2022).
- [23] M. Ragone, P. Braccia, Q. T. Nguyen, L. Schatzki, P. J. Coles, F. Sauvage, M. Larocca, and M. Cerezo, Representation theory for Geometric Quantum Machine Learning, [arXiv:2210.07980 \[quant-ph\]](https://arxiv.org/abs/2210.07980) (2022).
- [24] Q. T. Nguyen, L. Schatzki, P. Braccia, M. Ragone, P. J. Coles, F. Sauvage, M. Larocca, and M. Cerezo, Theory for Equivariant Quantum Neural Networks, [arXiv:2210.08566 \[quant-ph\]](https://arxiv.org/abs/2210.08566) (2022).
- [25] F. Sauvage, M. Larocca, P. J. Coles, and M. Cerezo, Building spatial symmetries into parameterized quantum circuits for faster training, *Quantum Sci. Technol.* **9**, 015029 (2024).
- [26] L. Schatzki, M. Larocca, Q. T. Nguyen, F. Sauvage, and M. Cerezo, Theoretical guarantees for permutation-equivariant quantum neural networks, [arXiv:2210.09974 \[quant-ph\]](https://arxiv.org/abs/2210.09974) (2022).
- [27] E. Grant, M. Benedetti, S. Cao, A. Hallam, J. Lockhart, V. Stojevic, A. G. Green, and S. Severini, Hierarchical quantum classifiers, *Npj Quantum Inf.* **4**, 1 (2018).
- [28] I. Cong, S. Choi, and M. D. Lukin, Quantum convolutional neural networks, *Nat. Phys.* **15**, 1273 (2019).
- [29] A. Pesah, M. Cerezo, S. Wang, T. Volkoff, A. T. Sornborger, and P. J. Coles, Absence of barren plateaus in quantum convolutional neural networks, *Phys. Rev. X.* **11**, 041011 (2021).
- [30] M. Schuld and N. Killoran, Is quantum advantage the right goal for quantum machine learning?, *PRX quantum* **3**, 030101 (2022).
- [31] H.-Y. Liu, Z.-Y. Chen, T.-P. Sun, C. Xue, Y.-C. Wu, and G.-P. Guo, Can variational quantum algorithms demonstrate quantum advantages? Time really matters, [arXiv:2307.04089 \[quant-ph\]](https://arxiv.org/abs/2307.04089) (2023).
- [32] K. Chinzei, S. Yamano, Q. H. Tran, Y. Endo, and H. Oshima, Trade-off between gradient measurement efficiency and expressivity in deep quantum neural networks, [arXiv:2406.18316 \[quant-ph\]](https://arxiv.org/abs/2406.18316) (2024).
- [33] K. Chinzei, Q. H. Tran, K. Maruyama, H. Oshima, and S. Sato, Splitting and parallelizing of quantum convolutional neural networks for learning translationally symmetric data, *Phys. Rev. Res.* **6**, 023042 (2024).
- [34] Y. LeCun, Y. Bengio, and G. Hinton, Deep learning, *Nature* **521**, 436 (2015).
- [35] A. Krizhevsky, I. Sutskever, and G. E. Hinton, ImageNet classification with deep convolutional neural networks, *Commun. ACM* **60**, 84 (2012).
- [36] Y. LeCun, Y. Bengio, and Others, Convolutional networks for images, speech, and time series, *The handbook of brain theory and neural networks* **3361**, 1995 (1995).
- [37] J. Herrmann, S. M. Lima, A. Remm, P. Zapletal, N. A. McMahon, C. Scarato, F. Swiadek, C. K. Andersen, C. Hellings, S. Krinner, N. Lacroix, S. Lazar, M. Kerschbaum, D. C. Zanuz, G. J. Norris, M. J. Hartmann, A. Wallraff, and C. Eichler, Realizing quantum convolutional neural networks on a superconducting quantum processor to recognize quantum phases, *Nat. Commun.* **13**, 4144 (2022).
- [38] Y.-J. Liu, A. Smith, M. Knap, and F. Pollmann, Model-independent learning of quantum phases of matter with quantum convolutional neural networks, [arXiv:2211.11786 \[quant-ph\]](https://arxiv.org/abs/2211.11786) (2022).
- [39] S. Monaco, O. Kiss, A. Mandarino, S. Vallecorsa, and M. Grossi, Quantum phase detection generalization from marginal quantum neural network models, *Phys. Rev. B.* **107**, L081105 (2023).
- [40] S. Y.-C. Chen, T.-C. Wei, C. Zhang, H. Yu, and S. Yoo, Quantum convolutional neural networks for high energy physics data analysis, *Phys. Rev. Res.* **4**, 013231 (2022).
- [41] L. Nagano, A. Miessen, T. Onodera, I. Tavernelli, F. Tacchino, and K. Terashi, Quantum data learning for quantum simulations in high-energy physics, *Phys. Rev. Res.* **5**, 043250 (2023).
- [42] M. Schuld, V. Bergholm, C. Gogolin, J. Izaac, and N. Killoran, Evaluating analytic gradients on quantum hardware, *Phys. Rev. A* **99**, 032331 (2019).
- [43] M. Larocca, P. Czarnik, K. Sharma, G. Muraleedharan, P. J. Coles, and M. Cerezo, Diagnosing barren plateaus with tools from quantum optimal control, *Quantum* **6**, 824 (2022), 2105.14377v3.
- [44] M. Ragone, B. N. Bakalov, F. Sauvage, A. F. Kemper, C. O. Marrero, M. Larocca, and M. Cerezo, A unified theory of barren plateaus for deep parametrized quantum circuits, [arXiv:2309.09342 \[quant-ph\]](https://arxiv.org/abs/2309.09342) (2023).
- [45] E. Fontana, D. Herman, S. Chakrabarti, N. Kumar, R. Yalovetzky, J. Heredge, S. H. Sureshbabu, and M. Pistoia, The adjoint is all you need: Characterizing Barren Plateaus in quantum ansätze, [arXiv:2309.07902 \[quant-ph\]](https://arxiv.org/abs/2309.07902) (2023).
- [46] J. J. Rotman, *An introduction to the theory of groups*, 4th ed., Graduate texts in mathematics (Springer, New

- York, NY, 2012).
- [47] D. P. Kingma and J. Ba, Adam: A method for stochastic optimization, in *3rd International Conference on Learning Representations, ICLR 2015, San Diego, CA, USA, May 7-9, 2015, Conference Track Proceedings*, edited by Y. Bengio and Y. LeCun (2015).
- [48] H. Robbins and S. Monro, A Stochastic Approximation Method, *Ann. Math. Stat.* **22**, 400 (1951).
- [49] M. Cerezo, M. Larocca, D. García-Martín, N. L. Diaz, P. Braccia, E. Fontana, M. S. Rudolph, P. Bermejo, A. Ijaz, S. Thanasilp, E. R. Anschuetz, and Z. Holmes, Does provable absence of barren plateaus imply classical simulability? Or, why we need to rethink variational quantum computing, [arXiv:2312.09121](https://arxiv.org/abs/2312.09121) [quant-ph] (2023).
- [50] G. Vidal, Entanglement renormalization, *Phys. Rev. Lett.* **99**, 220405 (2007).
- [51] G. Evenbly and G. Vidal, Class of highly entangled many-body states that can be efficiently simulated, *Phys. Rev. Lett.* **112**, 240502 (2014).
- [52] Y. Suzuki, Y. Kawase, Y. Masumura, Y. Hiraga, M. Nakadai, J. Chen, K. M. Nakanishi, K. Mitarai, R. Imai, S. Tamiya, T. Yamamoto, T. Yan, T. Kawakubo, Y. O. Nakagawa, Y. Ibe, Y. Zhang, H. Yamashita, H. Yoshimura, A. Hayashi, and K. Fujii, Qulacs: a fast and versatile quantum circuit simulator for research purpose, *Quantum* **5**, 559 (2021), [2011.13524v4](https://arxiv.org/abs/2011.13524v4).